Arab American University – Jenin

Faculty of Graduate Studies

Design and Characterization of $ZnSe/SeO_2$ Heterojunction Devices

By

Suzan Khaled Sulaiman

Supervisor

Prof. Dr. Atef Fayez Qasrawi

This thesis was submitted in partial fulfillment of the requirements for

The Master's degree in

Physics

May/2022

Design and characterization of $ZnSe/SeO_2$ heterojunction devices

By

Suzan Khaled Sulaiman

This thesis was defended successfully on 19th May 2022 and approved by:

Committee members	Signature
1. Prof. Dr. Atef Fayez Qasrawi : Supervisor	.....
2. Assoc. prof. Dr. Iyad Saadeddin : External examiner	.....
3. Prof. Dr. Hazem Khanfar : Internal Examiner	.....

Declaration

The work provided in this thesis, unless otherwise referenced, is the researcher's own work, and has not been submitted elsewhere for any other degree or qualification.

العمل المقدم في هذه الرسالة، ما لم تتم الاشارة الى غير ذلك، هو عمل الباحث الخاص ولم يتم تقديمه في أي مكان اخر للحصول على أي درجة أو مؤهل اخر.

Student's Name: **Suzan Khaled Sulaiman**

Signature: 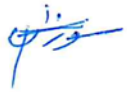

Data: 19-9-2022

Acknowledgments

In the name of God, the Most Gracious, the Most Merciful, and my success is only by Allah. My master's thesis has been completed from my prestigious university, Arab American University thanks to God. I extend my sincere thanks and appreciation to all faculty members. In particular, the honorable Professor Dr. Atef Qasrawi, who has spared no effort in order for the thesis to see the light. God rewarded him with the best reward ... And I also thanks to the external examiner, the virtuous Prof. Dr.Iyad Saadeddin and the internal examiner, the virtuous Prof. Dr.Hazem Khanfar.

All thanks and love to my beautiful family who supported me all the time. My little family (my dear partner Ibraheem and my beloved childrens). My big family (my dear parents, my sisters and brothers) ,whose prayers for me was the secret of my success ... My hope and happiness are you.

Thank are also due to the kind assistance Rana Daraghmeh who provided me with support and assistance, both in the practical and theoretical side throughout the work … My wonderful friend Salsabeel, who was distinguished by loyalty and giving, and we walked together on the path to success … Praise be to God, and we will continue. Thanks for my dear colleagues Lara, Wala, and Bayan who provided me with support and assistance.. Last but not least, all appreciation to all those who provided me the possibility to complete this work.

Design and Characterization of ZnSe/SeO_2 Heterojunction Devices

By

Suzan Khaled Sulaiman

Supervisor

Prof. Dr. Atef Fayez Qasrawi

Abstract

In this thesis we have designed and fabricated new class of heterojunction devices. n-ZnSe thin films are used as substrates to coat p-SeO_2. The formed pn junction is prepared by thermal evaporation technique under vacuum pressure of 10^{-4} mbar. In accordance with x-ray diffraction studies the films shows stacking of polycrystalline ZnSe and amorphous SeO_2. To construct the energy band diagram of the ZnSe/SeO_2 devices, the work function of SeO_2 was determined by electrical measurements. The band gaps of ZnSe and SeO_2 were also experimentally determined. In accordance with the designed energy band diagram ZnSe/SeO_2 heterojunctions exhibit conduction and valence band offsets of $1.91\ eV$ and $1.61\ eV$, respectively. The flat band build in potential is $0.59\ eV$ allowing formation of thin film transistor channels. When the ZnSe/SeO_2 interfaces are coated onto Ag metal substrates they show microwave resonators characteristics. Particularly, the capacitance spectra which is studied in the frequency domain $0.1 - 1.8\ GHz$ displayed negative capacitance effect accompanied with resonance-

antiresonance Phenominance. Modeling of the capacitance spectra using existing models have shown that SeO_2 layer improves the geometrical capacitance of ZnSe by more than 4 times. In addition, deep analysis of the ac current conduction in the microwave frequency domain have shown the current is dominated by the correlated barrier hopping and by the quantum mechanical tunneling. The density of fermi levels at the interface region reaches $10^{18} cm^3 eV$. Moreover, the device is found suitable for ac signal filtering. It show band stop filter characteristics with acceptable return loss values and voltage standing wave ratios. The Ag/ZnSe/SeO_2 devices can also be engineered by insertion of Ag nanosheets of 50 nm thickness between ZnSe and SeO_2. These nanosheets negatively affected the polycrystalline nature of the films but remove the negative capacitance effect of the devices. Ag nanosheets also increased the conductance in the spectral range of $0.5 - 1.5\ GHz$. Ag nanosheets decrease the density of states near Fermi level by two orders of magnitude. In general with these properties ZnSe/SeO_2 interfaces can be nominated as microwave resonators and negative capacitance sources.

List of Contents

List of Tables

List of Figures

List of Symbols

Symbol	Symbol Meaning
ZnSe	Zinc Selenide
SeO_2	Selenium dioxide
λ	Wavelength
D	Inter-planner distance
Θ	Bragg angle
N	Integer
Hkl	Miller indices
D	Crystallite size
β	Full width of the peak at half maximum (FWHM) measured in radians
ε	Lattice strain
δ	Dislocation density
SF %	Stacking faults
E_g	Energy band gap
A	Absorption coefficient
E_a	Activation energy
E	The electron charge
E	The electric field
W	The angular frequency
D	Electric displacement
Z	The impedance
QMT	Quantum mechanical tunneling
CBH	Correlated barrier hoping

Chapter One

Introduction

Zinc Selenide ZnSe has attracted researcher's attention due to its distinctive properties that make it of a major role in optoelectronic applications. It has been used in solar cell devices as a buffer layer [1]. ZnSe thin films exhibit p-type semiconducting nature at room temperature [2]. In addition, ZnSe thin films at higher incident power intensities of light exhibit better optical limiting responses that promise for use it as optical limiters [3]. Moreover, ZnSe giving the photonic bandgap properties for silica optical fiber claddings indicate the possibility of generating new class of optical fibers [4]. In one of the reports, ternary ZnSeTe quantum dots used ZnSe as a double shell with ZnS to get ZnSeTe/ZnSe/ZnS hetero structure. Quantum dot light emitting diodes of high electroluminescence performances being effective in the ranges of 6107-12654 lum revealed an external quantum efficiency of 5.3-18.6 % [5].

ZnSe thin films were prepared in many methods. Selenization is a method for preparing ZnSe films on quartz substrates by selenizing as-sputtered ZnSe films at different temperatures for 6 hours [6]. Chemical bath deposition method (CBD) was also used for preparing ZnSe thin films. Namely, films are produced by deposition in acidic solutions for various deposition times [7]. ZnSe films were also deposited by employing e-beam evaporation technique to study its induced physical properties under thermal annealing for buffer layer in solar cells [8]. Radio frequency magnetron sputtering is also used for deposition of ZnSe onto optical glass and onto indium-tin-oxide (ITO) coated glass substrates [9].

Structural analysis of ZnSe showed that it exhibits a cubic structure with preferred orientation along the plane of (111) [10], with optical bandgap ranging from 2.69 to 2.81 eV [9]. The structure morphology and optical properties of the ZnSe had been affected significantly by the annealing [11]. Films deposited by photo-assisted chemical bath deposition (PCBD) for longer annealing times are observed to have a decreasing selenium and increasing zinc contents [11]. ZnSe films deposited by e-beam evaporation technique displayed a decrease in refractive index with increasing temperature [12]. Increasing in the binding energy of ZnSe was also observed with the increase in structural size [13]. The mobility of the ZnSe films grows up from 255 to 1250 cm^2/Vs as the film thickness increases from 30 to 90 nm [14]. Synthesized and annealed films (at various temperatures), revealed a transmittance of more than 80 %, and reduction in strain and dislocation density [15]. The ZnSe band gaps decrease with increase in the hydrazine hydrate volume that used for deposition [16]. The deposited thin films color emissions is influenced is by changing the hydrazine hydrate volume [16]. ZnSe doped with cobalt showed electrical conductivity of 6.3×10^{-6} - 5.47×10^{-5} $(\Omega\, cm)^{-1}$ [17].

Another material that occupy its position in literature and attracted attention is Selenium dioxide (SeO_2). This material show smart features . SeO_2 plays a role as selectrocatalyst for long stable water splitting process [18]. SeO_2 has a role in spectrophotometric determination of tetracline drug in pure and pharmaceulrical formulations [19]. SeO_2 is one of the oxides involved in the a newly developed PhO-B_2O_3-SeO_2-Er_2O_3:Au_2O_3 glass ceramic that has a big chance to use for gamma ray based applications [20].

However, reports on the optical and electrical properties of SeO_2 in the thin films form are relatively rare. No information is available about its electrical resistivity

and/or conductivity. Our early observations have shown that SeO_2 is a very transparent material and can be used as oxide layer in semiconductor devices.

The special properties for these important semiconductors motivated us to explore the performance of ZnSe/SeO_2 hetero junction. For this reason, thin film of ZnSe/SeO_2 of thickness 1000 nm is coated onto 1000 nm Ag substrates coated on glass slides. ZnSe-SeO_2 structural, and electrical properties are studied by x-ray diffraction and impedance spectroscopy techniques, respectively. The changes that occurred to ZnSe after adding SeO_2 layer to form the hetero junction ZnSe/SeO_2 will be mentioned in details. In addition, preliminary electrical analysis for the properties of the ZnSe/SeO_2 heterojunction monitored smart features that are encouraging it to have a major role in the recent electronic applications.

ZnSe/SeO_2 heterojunction is prepared by thermal evaporation technique, In the current work, the structural and electrical properties of ZnSe/SeO_2 heterojunction are analyzed and studied. The structural properties will be analyzed through X-ray diffraction technique with the help of Miniflex-600 XRD unit. The optical measurements will allow to construct band diagram. The electrical properties will be studied via impedance spectroscopy through utilization of Agilent impedance analyzer. The dc electrical measurements will allow the determination of the work function of SeO_2.

In this thesis, Chapter two includes theoretical background, chapter three contains experimental details, chapter four displays our results and discussions including structural, morphological, optical, impedance spectroscopy and current – voltage characteristics analysis. And chapter five will report the remarkable conclusions.

Chapter 2

Theoretical Background

2.1 The X-ray Diffraction

X ray diffraction is an important tool for structural and phase composition studies. Its introduces the clear information about the nature of the composition, the atomic structure of crystalline substances, and the preferred crystal orientations, x ray diffraction distinguish the crystalline material from amorphous one [21].

2.1.1 Bragg's law

X ray diffraction represented how the x ray photons scattered elastically by atoms in periodic lattice, constructive interference produced when the interactions between the incident rays and the sample satisfying the conditions of Bragg's law [22].

$$2d \sin\theta = n\lambda \qquad (2.1)$$

Where λ is the wavelength of the x ray 1.5405 Å, θ is the diffraction angle, n is an integer, d is the inter planer spacing between two planes of atoms.

By combining the Bragg's condition with obtained inter planer spacing, the lattice parameters of the individual plane with Miller indices hkl assuming the cubic crystal system are revealed by the equation[23]:

$$\frac{1}{d_{hkl}^2} = \frac{1}{a^2}(h^2 + k^2 + l^2) \qquad (2.2)$$

2.1.2 Crystallography

The crystal is a three dimensional arrangement of atoms as pattern repeats periodically. The periodicity is the most important feature of the crystal. Materials in crystalline state contains atoms arranged in planes with inter planer spacing d. The basic building unit of the crystal is the unit cell. The shape and size of a unit cell can be determined by the three independent edges a, b, and c, and the three angles in between α, β and γ [24]. The reciprocal of fractional intercept of the planes on the edges of the unit cell called Miller indices. It is important to consider a whole family of parallel and identical planes forms the crystal [25]. The atoms on crystal can be arranged in seven structures through fourteen of 3 dimensional configurations, called Braves lattice [25]. the groups of the main Bravais lattice are represented in Table 2.1. the fourteen Bravais lattices are represented in Table 2.2

Table 2.1 The 7 lattice groups in three dimensions.

System	Number of lattices	Restrictions on conventional cell axes and angles
Triclinic	1	$a \neq b \neq c$, $\alpha \neq b \neq \gamma \neq 90^0$
Monoclinic	2	$a \neq b \neq c$, $\alpha = b = 90^0 \neq \gamma$
Orthorhombic	4	$a \neq b \neq c$, $\alpha = b = \gamma = 90^0$
Tetragonal	2	$a = b \neq c$, $\alpha = b = \gamma = 90^0$
Cubic	3	$a = b = c$, $\alpha = b = \gamma = 90^0$
Trigonal	1	$a = b = c$, $\alpha = b = \gamma < 120^o \neq 90^0$
Hexagonal	1	$a = b \neq c$, $\alpha = b = 90^0$, $\gamma = 120^o$

Table 2.2 The 14 lattice types in three dimensions.

System	Bravais Lattice			
Cubic	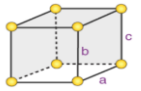 Simple Cubic	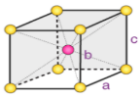 Body centered cubic	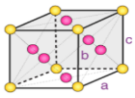 Face centered cubic	
Orthorhombic	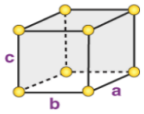 Simple Cubic	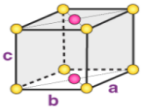 Base centered cubic	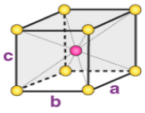 Body centered cubic	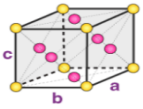 Face centered cubic
Tetragonal	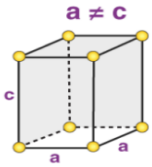 Simple	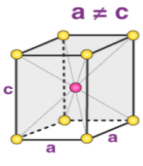 Body centered		
Monoclinic	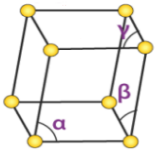 Centered	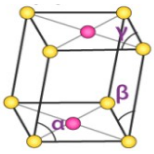 Simple		
Triclinic	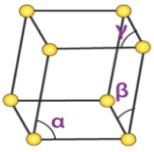 Simple			
Trigonal	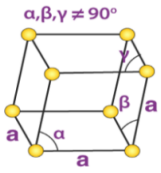 Simple			
Hexagonal	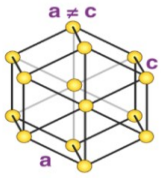 Simple			

2.1.3 Structural Parameters

Through x ray diffraction patterns, many important structural parameters obtained from the most intensive peak, by using its broadening width β. These parameters are:

i. Strain (ε) : change into bond length with respect to its original length, which affect the orientation of the crystal [26], and found using,

$$\varepsilon = \frac{\beta}{4\tan(\theta)} \tag{2.3}$$

ii. "Crystallite" size (D): is the diameter of individual crystalline, which expresses the size of it [26], from the following equation,

$$D = \frac{0.94\,\lambda}{\beta\cos(\theta)} \tag{2.4}$$

iii. Dislocation density (δ): expresses concentration of dislocation in the crystal, it is measured by counting the number of dislocation lines that cross a unit area of surface, measured in lines/cm^2 [26], using,

$$\delta = \frac{15\,\varepsilon}{aD} \tag{2.5}$$

iv. Stacking faults (SF): are crystallographic defects So that the correct arrangement of the stacking planes is interrupted [26], expressed by,

$$SF = \frac{2\,\pi^2\beta}{45\sqrt{3\tan(\theta)}} \tag{2.6}$$

2.2 Optical Properties

The diversity of optical properties of semiconductor materials indicates a great opportunity to use in optoelectronic applications.

2.2.1 Optical Processes Characterization

The main optical processes encloses reflection, propagation and transmission. When a light beam entering to a medium from vacuum, the incident beam will reflects from the front surface or propagates through the medium until reaches the back surface. At the back surface, the light may be reflected or transmitted outside the medium. The four processes of linear optical propagation are scattering , absorption, luminescence and refraction.

Refraction is the change in the light direction as it is travel from one medium to another. Refraction is the bending of light when it enters a medium where it has a different speed. The bending of the path of a light wave is described by Snell's law [27].

$$n_1 \sin\theta_1 = n_2 \sin\theta_2 \qquad (2.7)$$

The numbers in equation (2.7) refer to the mediums.

2.2.2 Absorption of Light in Matter

Analysis of optical absorption scale is one of the most dominant techniques to get information about the band construction and energy gap (E_g) of semiconductor materials. Absorption is engaged with photon-electron interaction**.** When an incident photon is taken by the optical medium, it causes electron to move from the valence to conduction band. The light absorption of the material is resolved by the absorption

coefficient (α), which reveals the rate of incident light intensity attenuation over the propagated distance.

By reason of the photon momentum $\left(\frac{h}{\lambda}\right)$ is lower than the crystal momentum $\left(\frac{h}{a}\right)$, electron momentum is continued conservative equable when the photon is absorbed.

The transmittance of light on condition of two parallel surfaces is gained by the following expression [28],

$$T = (1 - R_1)e^{-\alpha d}(1 - R_2) \tag{2.8}$$

Where $R_1$and R_2 describe the reflectivity's of the head and back film surface and d is the medium depth . If $R_1 = R_2$, equation (2.8) become [29],

$$T = (1 - R)^2 e^{-\alpha d} \tag{2.9}$$

When three materials are emplaced onto glass substrate, the phrase $(1 - R_3)$ should be added in the equation (2.8).

The transmittance of the multilayer film able to be written as,

$$T = \frac{(1 - R_1)(1 - R_2)e^{-\alpha d}}{1 - R_1 R_2 e^{-2\alpha d}} \tag{2.10}$$

After monitoring the film depth (d), the Absorption coefficient $\alpha(h\upsilon)$ can be resolved from the following relation [30],

$$\alpha = \frac{-\ln\left(\frac{T}{(1 - R_{glass})(1 - R_{sample})}\right)}{d} \tag{2.11}$$

2.2.3 Band Gap Calculations

The energy gap is named by using the spectrophotometric absorption spectrum incapable to understand and obtain more foretelling information about solids characteristics. For this purpose, Tauc's equation, which connect between spectrophotometric absorption coefficient and the incident photon energy is applied. This equation shows that the energy band gap of the material is direct proportion to $(\alpha E)^{1/p}$ as specified in the subsequent equation [31],

$$(\alpha E)^{1/p} = B\left(E - E_g\right) \tag{2.12}$$

Where E is the incident photon energy, p is an index that gives the class of the optical absorption mechanism and it able to have the values 2, 1/2, 3, and 3/2 for indirect allowed, direct allowed, indirect forbidden and direct forbidden electronic transition, consequently. B is a constant that is mainly depends on the transition chance of electron, and E_g illustrates the energy gap.

The E_g of the material can be determined among $(\alpha E)^{1/p}$ plotting contrary to the incident photon energy E. The graph which represents a widest range of linear data in the high absorption part is then selected. The linear section of $(\alpha E)^{1/p}$ can be deduced and the energy gap for semiconductor materials can be resolved from the intercept of the $E - axis$.

2.3 Impedance Spectroscopy

Electrical impedance represents the ability to prevent the flowing of the electrical current through the multi-element circuit when an AC voltage is applied. The impedance is a function of the frequency of the sinusoidal applied voltage

$$Z(\omega) = \frac{V(\omega)}{I(\omega)} \tag{2.13}$$

and it is measured in SI units by ohm (Ω).

2.3.1 Series RLC Circuits

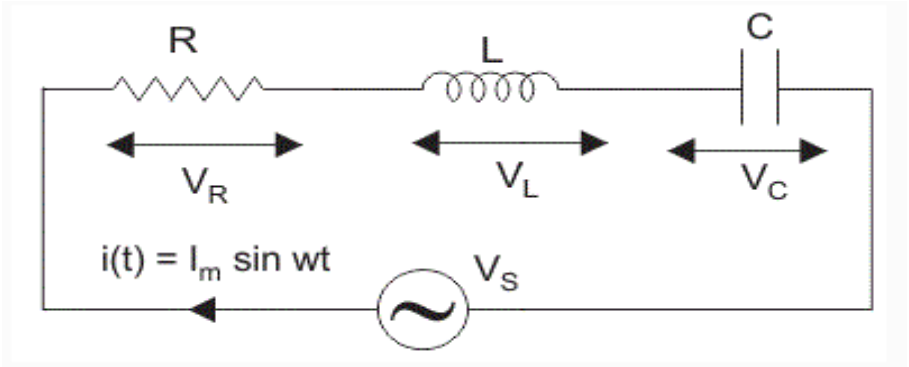

Fig. 2.1. Series RLC circuit.

Series RLC Circuits contains the most basic elements which are a resistor, inductor and capacitor joined across voltage supply. All these elements share in being energy consuming more than producing, and all of them have a linear relationship between current and voltage. In series RLC circuits, the resistor, inductor and capacitor are connected in series with power supply Fig 2.1. Accordingly, the currents in the resistor (I_R), inductor (I_L) and capacitor (I_C) are the same, where the voltage is the mathematical sum of the resistor voltage (V_R), inductor voltage (V_L), capacitor voltage (V_C), because V_R is in phase with the current while V_L leads the current by 90°, V_C lags the current by 90° as shown in Fig 2.2.

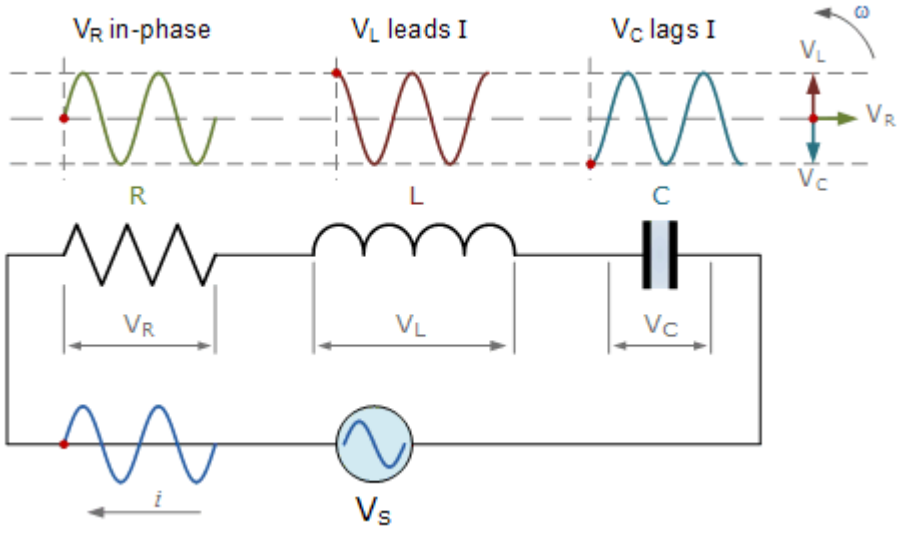

Fig. 2.2 The series RLC circuit.

Where

$$V_r = IR \tag{2.14}$$

$$V_L = I\chi_L \tag{2.15}$$

$$V_C = I\chi_C \tag{2.16}$$

R is the resistance of the resistor, χ_L is the inductive reactance, χ_C is the capacitive reactance, both of the χ_L and χ_C are functions of the source frequency (ω), and given by:

$$\chi_L = j\omega \tag{2.17}$$

$$\chi_C = \frac{1}{\omega C} \tag{2.18}$$

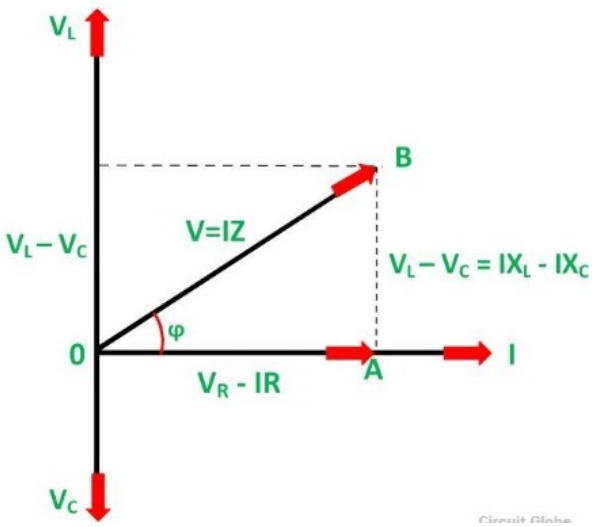

Fig. 2.3. The voltage triangle of a series RLC circuit.

The total voltage is the vector sum of V_R, V_L and V_C as shown in total phasor diagram for the series RLC circuit (Fig 2.3). It is then given by

$$V = V_R + V_L + V_C \tag{2.19}$$

With the magnitude of

$$|V| = I\sqrt{(R)^2 + (\chi_L - \chi_C)^2} = I\,Z \tag{2.20}$$

Where $Z = \sqrt{(R)^2 + (\chi_L - \chi_C)^2}$ is the impedance of series RLC circuit with phase angle φ, which can be found from

$$\cos(\varphi) = \frac{R}{Z}, \qquad \sin(\varphi) = \frac{(\chi_L - \chi_C)}{Z}, \qquad \text{or} \quad \tan(\varphi) = \frac{(\chi_L - \chi_C)}{R} \tag{2.21}$$

2.3.2 Frequency Dependent Conductivity

The conductivity formula is invariable with ac frequency signal (ω) through relation [32].

$$\sigma(\omega) = A\omega^s \tag{2.22}$$

Where A is constant, and s have value less than or equal unity. This behavior of AC conduction needs a wide range of relaxation time τ among loss mechanisms. The conductivity is linearly dependent on frequency if the distribution of relaxation time $n(\tau)$ is inversely proportional to τ, that requires

$$\tau = \tau_o e^{\xi} \tag{2.23}$$

Where ξ is random variable, τ_o is a characteristic relaxation time, equals to the inverse of phonon frequency ν_{ph}^{-1} [32].

In general, there are two current conduction mechanisms, quantum mechanical tunneling $\sigma_{Tunneling}(\omega)$, and correlated barrier hoping $\sigma_{CBH}(\omega)$, one or both may be present, so the total conductivity is [33]:

$$\sigma_T(\omega) = \left(\sigma_{Tunneling}^{-1} + \sigma_{CBH}^{-1}\right)^{-1} \tag{2.24}$$

For situation where quantum mechanical tunneling dominate, $\xi = 2\alpha R$, as for the situation in which correlated barrier hoping dominate $\xi = \exp\left(-\frac{E_H}{kT}\right)$, where R is the inter sited separation, α^{-1} is the spatial decay parameter, it is assumed to be constant ($\alpha^{-1} \approx 10A^o$), it is describes the localized state for each site and E_H is the hopping barrier hight [33].

Quantum mechanical tunneling and correlated barrier hoping conductivities are respectively given by

$$\sigma_{Tunneling}(\omega) = \frac{\pi^2}{24} kT\alpha^{-1}\left(N(E_F)\right)^2 \omega R_\omega^2 \tag{2.25}$$

$$\sigma_{CBH}(\omega) = \sigma(H) + \frac{\sigma(L) - \sigma(H)}{1 + (\omega\tau_n)^2} \tag{2.26}$$

Equations (2.25), (2.26), expressed quantum mechanical tunneling, correlated barrier hopping, respectively. In equation (2.25), R_ω is the hopping distance at a particular frequency calculated by $\frac{1}{2\alpha}\ln(\frac{1}{\omega\tau_o})$, $N(E_F)$ is the density of localized states at the fermi level. In equation (2.26), $\sigma(H)$, $\sigma(L)$ relate to the high- and low- frequency conductivity values, respectively, and $\tau_n = \tau_o \exp\left(-\frac{E_H}{kT}\right)$. The frequency dependence of $\sigma(\omega)$ as present in equation (2.25) can be reached by taking the derivative

$s = dln(\sigma(\omega))/dln(\omega)$, which has a value

$$s = 1 - \frac{4}{\left(\frac{1}{\ln(\omega\tau_O)}\right)} \qquad (2.27)$$

in situation where quantum mechanical tunneling dominate, the quantum mechanical tunneling satisfied when s is decreases with increasing in frequency [33].

2.3.3 Qasrawi – Ershov Model for Negative Capacitance Effect

In order to describe the capacitance spectra, Qasrawi - Ershov model was taken into consideration. According to this approach, the total capacitance contain of geometric part (C_o) and relaxation part (C_1) [34], in the form :

$$C(\omega) = C_o + C_1 \qquad (2.28)$$

The relaxation part C_1 is attributed to the impact ionization, trapping, carrier injection, electron transport and other physical processes. At certain voltage value, C_1 is determined by charge (ΔQ) motion which results in transient relaxation current $\delta_j(t)$ and can be expressed by the following equation [35],

$$C_1 = \frac{\Delta Q}{\Delta \mathrm{V}} = \frac{1}{\Delta \mathrm{V}} \int_0^{\infty} \delta_j(t) \cos(\omega - \omega_{1,2}) t dt$$

$$= \frac{1}{\omega \Delta \mathrm{V}} \int_0^{\infty} (-\frac{d\, \delta_j(t)}{dt}) \sin(\omega - \omega_{1,2})\, t dt \qquad (2.29)$$

This approach assumes that there are two different frequency domains (ω, ω_1) and $(\omega - \omega_2)$, as that ω_1, ω_2 indicates to the limits of frequency domains in the electron and hole regions, respectively. charge transport from both sides of the device result in transient response which is assumed to be composed of negative and positive exponential components.

The transient current is described by the following formula [35],

$$\delta_j(t) = \Delta \mathrm{V} \left(a_1 \exp\left(-\frac{t}{\tau_1}\right) - a_2 \exp\left(-\frac{t}{\tau_2}\right) \right) \qquad (2.30)$$

$C(\omega)$ equation will take the form:

$$C(\omega) = C_o + \frac{a_1 \tau_1}{1 + (\omega - \omega_1)^2 \tau_1^2} - \frac{a_2 \tau_2}{1 + (\omega - \omega_2)^2 \tau_2^2} \qquad (2.31)$$

In equation (2.31), τ_1, τ_2 are related to relaxation time of electrons and holes, respectively. Where a_1 and a_2 are the pre-exponential factors in F/s, It expresses the rate of change of dynamic capacitance with time

The value of the transient current control that the capacitance will be negative or positive. If $\delta_j(t)$ exhibits positive value and decreases monotonically reaches zero at $t \to \infty$ then, $C_1 > 0$ and $C(\omega) > C_o$ at any frequency. This indicates a positive value of $-\frac{d\, \delta_j(t)}{dt}$ and a monotonically decreases to zero. In this case, the positive contribution to the integral which exist at the right side of equation (2.29) over the

first half of a sine period dominates the negative contribution over the second half of the period .Furthermore, if the function $-\frac{d\,\delta_j(t)}{dt}$ is negative and monotonically increasing to zero, then the integral in the right side of the equation (2.29) is negative and $C(\omega)$ has a negative value. The capacitance can be negative in limited frequency ranges in the case of nonmonotonic or the derivative of the transient current has a positive valued behavior. This approach state that, the origin of the negative capacitance is assigned to the nonmonotonic or positive-valued behavior of the derivative of the transient current as a reaction to a small voltage step [35]. The capacitance is directly dependent on the degree of polarization that represented by dielectric constant. when an AC signal frequency is imposed into the material, electric dipoles response to the alternating field by oscillating. The static mode of dielectric constant exist in situation of C_o domination, when plasmon frequency $\omega_1\ and\ \omega_2$ are larger than AC incident frequency ω [36].

Responding of all dipoles to alternating current signals start when the value of incident AC frequency ω become close to plasmon frequency $\omega_1\ and\ \omega_2$. At particular frequency, when ω equals to $\omega_1\ and\ \omega_2$, then there is no free charge observed and all diploes oscillate with the field. In that case, resonance – anti resonance phenomena occurs [36].

Chapter Three

Experimental Details

3.1 Glass Cleaning

All the prepared thin films are deposited on glass slides. For this, glass must be very clean in order to prevent contaminations with contaminants. The process of cleaning the glass slides of dimensions of 25.4×76.2 mm and of thicknesses of 1.2 mm started by washing the glass slides with distilled water and alcohol, then placing the slides in a peaker of H_2O_2 (hydrogen peroxide), so that they were completely submerged and well covered with aluminum foil. Then they were placed in an ultrasound shaker for 25 minutes at a temperature of 70° C. After sterilization the glass slides ultrasonically, they were re-washed with distilled water again and then placed in a container of alcohol, and the container was immersed and covered with aluminum foil and placed in an ultrasound for the second time at room temperature for 30 minutes. After that, the glass slides were placed in a new container of alcohol covered with aluminum to keep them clean and ready for using as substrate of the thin films prepared by evaporation deposition.

3.2 Thin Film Preparation

In this thesis, all thin films are prepared by thermal evaporation technique using NORM VCM-600 evaporator (Fig 3.2.) under a vacuum pressure of 1.5×10^{-4} mbar. INFICON STM-2 thickness monitor was used to monitor the film thickness.

High purity Zinc Selenide powders (99.999% metal basis from Alfa Aesar) which are shown in Fig 3.2 are used as a source materials for preparing ZnSe thin films. The ZnSe were grown onto $1\ \mu m$ Ag substrates. Prior to ZnSe thin film coating, a 20 mg

of ZnSe powder is situated in a tungsten boat specialized for ZnSe. A 500 nm thick ZnSe films are prepared from ZnSe. The evaporation process of ZnSe took 7.0 min with an evaporation rate of $16.75\ A^{\circ}/sec$.

Fig. 3.1 The VCM-600 evaporation system.

Fig. 3.2 The ZnSe powders used to prepare the films.

In order to fabricate Ag/ZnSe/Ag (50 nm)/ SeO_2 thin film, silver powders were used as a source of Ag. A layer of Ag of 50 nm thick was deposited onto some of Ag/ZnSe thin films. SeO_2 layer was deposited onto part of the Ag/ZnSe and Ag/ZnSe/Ag(50

nm) films to prepare ZnSe/SeO_2 heterojunctions. Selenium dioxide powders (99.999% metal basis from Alfa Aesar) shown in Fig 3.3 are used as a source to prepare SeO_2 layers. For this purpose, a 20 mg of SeO_2 powders is situated in a tungsten boat specialized for SeO_2. A 500 nm thick of SeO_2 thin films in addition to the ZnSe/SeO_2 devices from SeO_2 powder were prepared. The evaporation rate was $10 A^{\circ}/sec$ for an evaporation duration of 10 min. The geometrical design of the produced films and heterojunction in addition to the optical images are shown in Fig 3.4 and Fig 3.5, respectively.

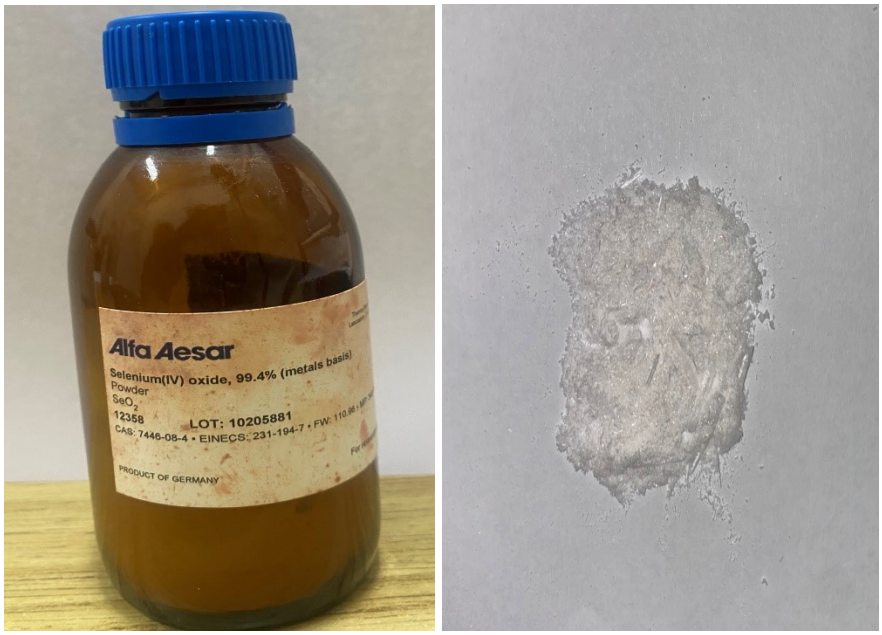

Fig. 3.3 The SeO_2 powders used to prepare the films.

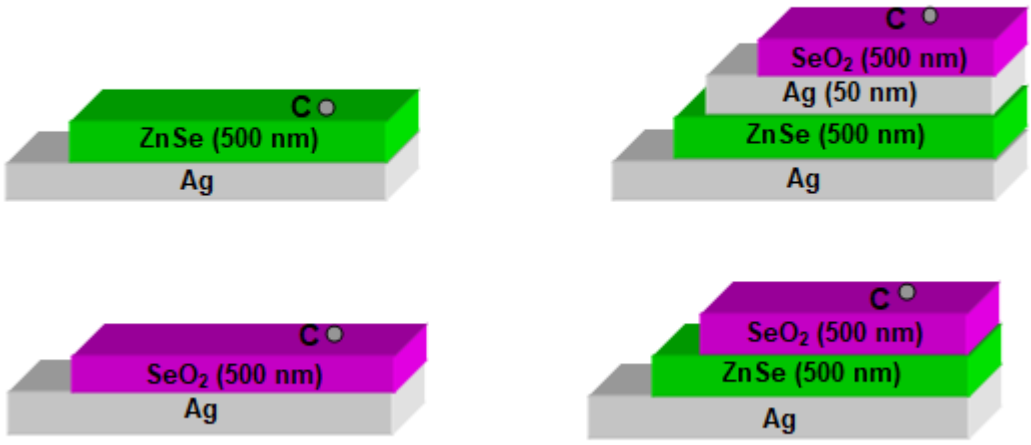

Fig. 3.4 The geometrical design of Ag/ZnSe/C, Ag/SeO_2/C, Ag/ZnSe/SeO_2/C and Ag/ZnSe/Ag (50 nm)/SeO_2 /C thin films.

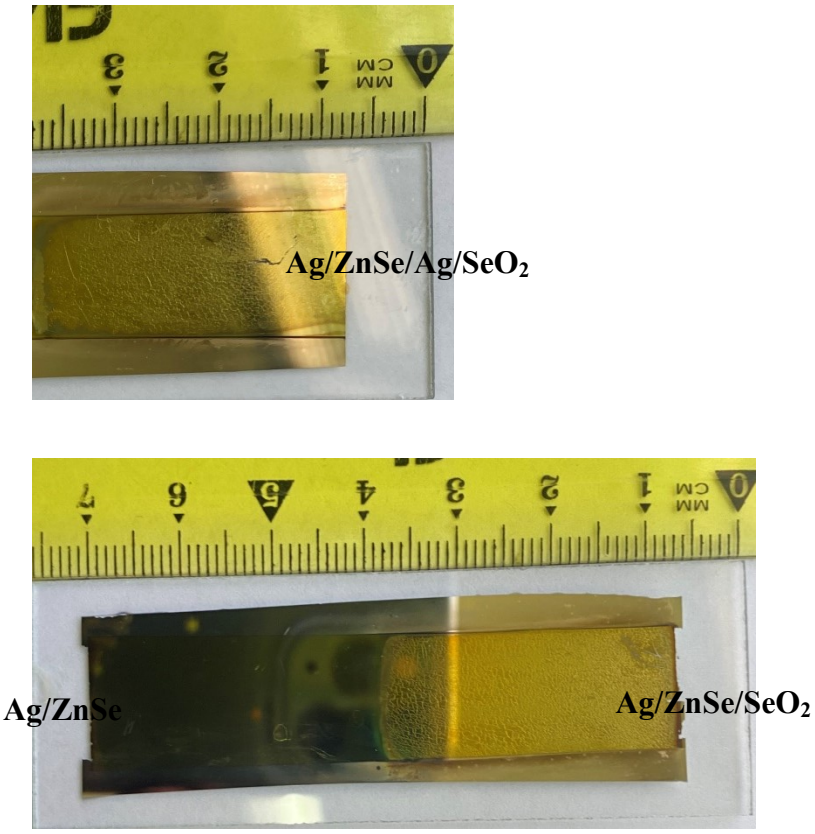

Fig. 3.5 The optical images of real thin films of Ag/ZnSe/C, Ag/ZnSe/SeO_2 /C and Ag/ZnSe/Ag (50 nm)/SeO_2 /C thin films.

3.3 Thin Film Analysis

Scanning electron microscope (SEM), X-ray diffraction (XRD), hot probe techniqe, optical measurements, impedance spectroscopy measurements , and electrical measurements were used to investigate the morphological, structural, conductivity type, optical properties, and electrical properties for the prepared thin films. These techniques are described in the following sections.

3.3.1 The Scanning Electron Microscopy (SEM) Measurements

In order to examine the film morphology, size, and uniformity of the prepared thin films, scanning electron microscopy technique was used with help of COXEM 200 scanning electron microscope Fig 3.6. SEM scans the surface of the samples by focusing a beam of energetic electrons of wide range of energy spectrum 0 - 40 keV . The electron beam is created by the field emission gun, through its inelastic collisions with the surface, the secondary electrons are produced. These electrons are in turn liberated and attracted to low potential before accelerated towards detector.

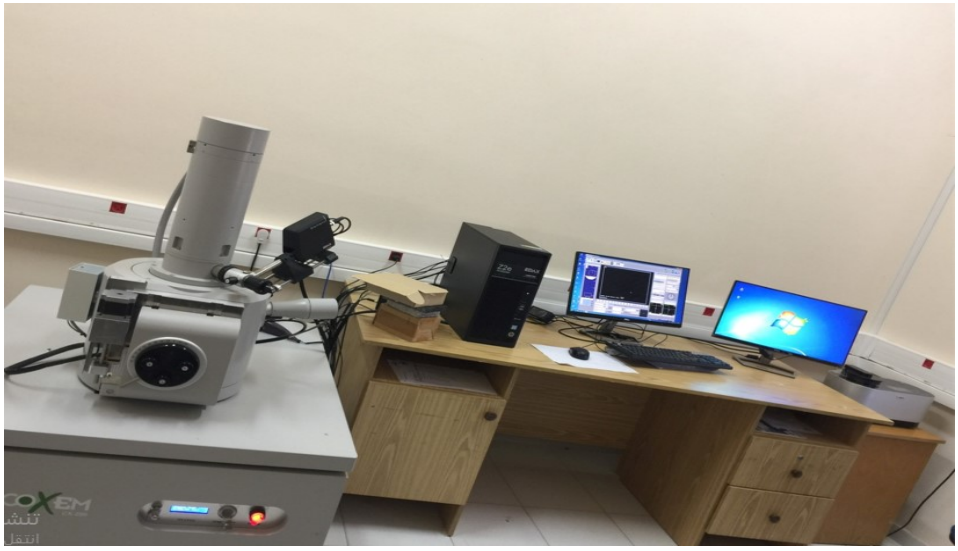

Fig 3.6. Scanning electron microscopy

3.3.2 The Hot Probe Technique

The hot probe technique which is shown in Fig 3.7 is used to evaluate the majority of charged carriers in the semiconductor thin films (n-conductivity or p-conductivity) , which determines the possibility of using in the electronic devices. The hot probe technique is a simple and efficient technique uses heated probe and standard multimeter. Two of probes (cold and hot) were attached to the surface of semiconductor, in which the cold probe was connected to the negative terminal of the multimeter and kept constantly attached to the surface of semiconductor, while the hot probe was connected to the positive terminal of the multimeter, and moving on the surface of the semiconductor, When the value of the voltage read out in the multimeter is positive, then the sample is n-type semiconductor, whereas the negative voltage represents p-type semiconductor. We have observed that ZnSe exhibits n-type of conductivity, whereas SeO_2 exhibits p-type.

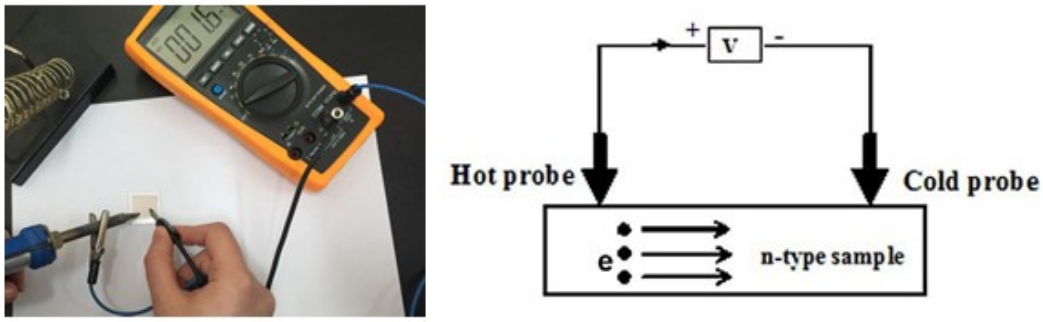

Fig. 3.7 The set-up of hot-probe technique.

3.3.3 The X-ray Diffraction (XRD) Measurements

The produced Ag/ZnSe, Ag/SeO_2 and Ag/ZnSe/SeO_2, Ag/ZnSe/Ag (50 nm)/SeO_2, films are structurally characterized by Rigaku MiniFlex-600 X-ray diffraction unit Fig

3.8 , a $K\alpha$ radiation source was the source of generated X rays, X rays generated has an average wavelength of 1.5404 A° at working voltage of at 40 kV, and with beam current of 15 mA. XRD patterns were recorded with scanning speed of 0.5°/min and scanning step of 0.05. The scan method was set in the $2\theta\ range\ of\ 10^{o} - 70^{o}$. In order to control instrument and process data a PC is used. The Bragg's diffraction law ($n\lambda = 2d\sin\theta$) was relied on to analyze the diffraction patterns, here λ is the wavelength of the X-ray used , and d is the distance between the planes, θ is half of the angle at which diffraction take place.

Fig. 3.8 X-ray Rigaku diffractometer.

3.3.4 Optical Measurements

The optical properties of the samples were measured using Thermoscientific Evolution 300 ultraviolet–visible light spectrophotometer (Fig. 3.9). The measurements have taken in the spectral wave length range of 300–1100 nm. The xenon (Xe) lamp inside the device emits light of different frequencies correspond to the spectrum of interest. The scanning speed of 1200 $nm/mins$.

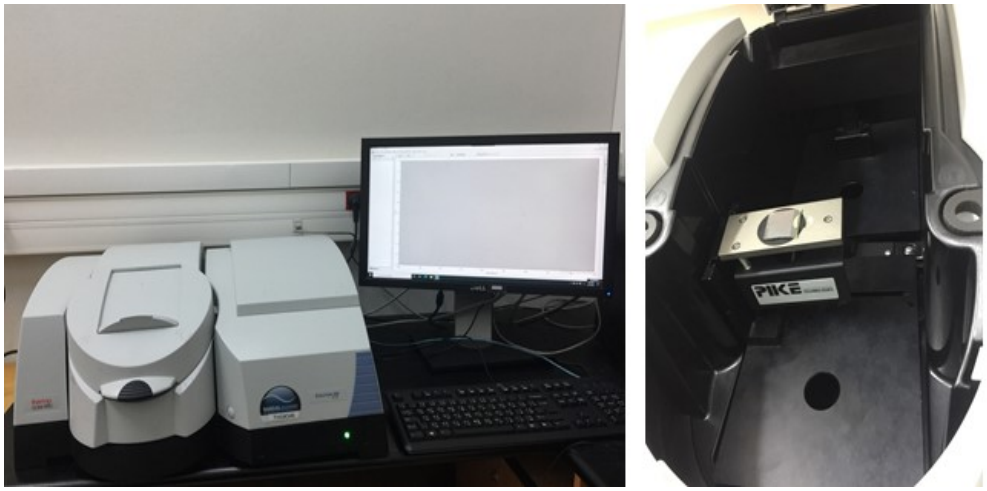

Fig. 3.9 The UV-VIS spectrophotometer

3.3.5 Impedance Measurements

The impedance spectroscopy measurements for Ag/ZnSe/C, Ag/ZnSe/SeO_2/C, and Ag/ZnSe/Ag (50 nm)/SeO_2/C heterojunction devices were carried out with the help of the Agilent 4291B 0.01–1.80 GHz impedance analyzer (Fig 3.10). The impedance, conductance, capacitance, and reflection coefficients of the target devices was measured in the frequency range $10 - 1800\ MHz$ by imposing an AC signal (of amplitude ~ 100 mV), then the data collected by the help of MATLAB software packages.

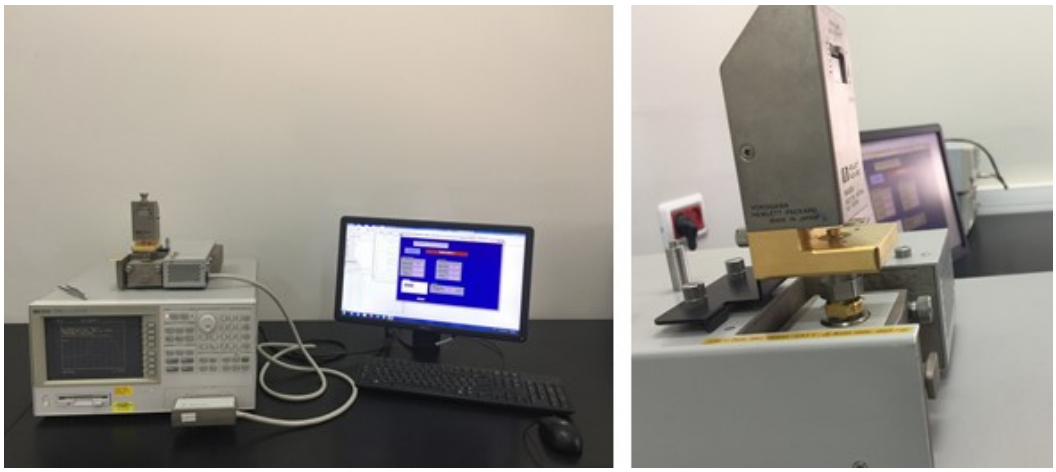

Fig. 3.10 The Agilent 4291B 0.01–1.80-GHz impedance analyzer.

3.4 Electrical Resistivity Measurements

To determine the work function of SeO_2, the temperature dependent electrical resistivity was recorded. A sample of SeO_2 thin films of thickness of 0.5 μm coated onto a glass substrates was used. The measured samples were of Hall bar shaped which is characterized by long, narrow shaped . The measurements were carried out using a homemade high temperature cryostat. The cryostat is composed of aluminum bar with flat end, K- type thermocouple, current –voltage characteristic system and Nickrome heating coil. The measurements were carried out in the temperature range of $290 - 410\ K$. The experimental setup is shown in Fig 3.11.

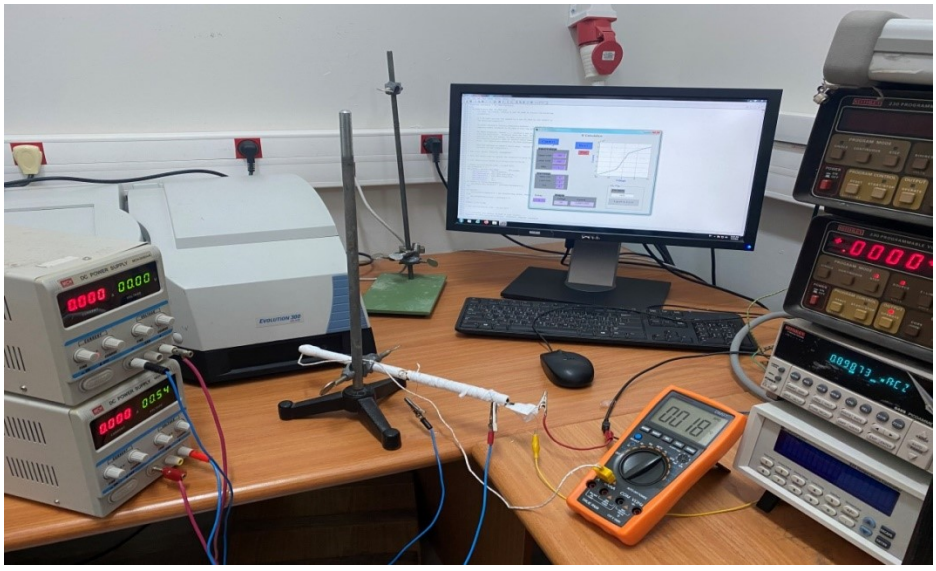

Fig. 3.11 The setup of high temperature cryostat and related apparatus.

3.5 Current – Voltage Measurments

In order to measure electrical properties, a carbon contact point was painted on top of ZnSe, ZnSe/SeO_2, and ZnSe/Ag (50 nm)/SeO_2 thin films which were deposited on Ag substrates. The current-voltage characteristics of the Ag/ZnSe/C, Ag/ZnSe/SeO_2/C and Ag/ZnSe/Ag(50 nm)/SeO_2/C devices were measured in the dark by means of

Keithley current–voltage characteristics system composed of Keithley 6485 Picoammeter and Keithley 230 voltage source Fig 3.12 . This in turn where connected to a PC by $IEEE - 488$ card, and controlled using MATlab software packages.

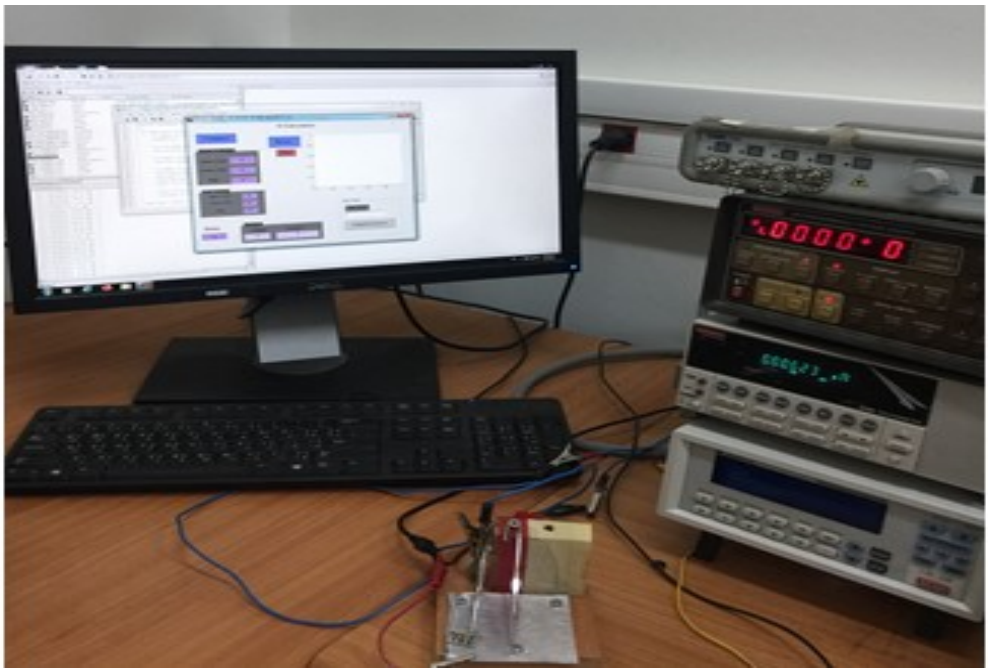

Fig. 3.12 The experimental setup of the I-V system in the dark.

Chapter Four

Results and Discussion

4.1 Structural Analysis

The structural analysis which identify the nature of the grown films was carried out with the help of X-ray diffraction unit operative at beam of power of 600 $watt$.

4.1.1 X-Ray Diffraction

The x-ray diffraction patterns of ZnSe, SeO_2, and ZnSe/SeO_2 and ZnSe/Ag(50 nm)/SeO_2 thin films deposited on 1μm Ag substrates are presented in Fig 4.1 .

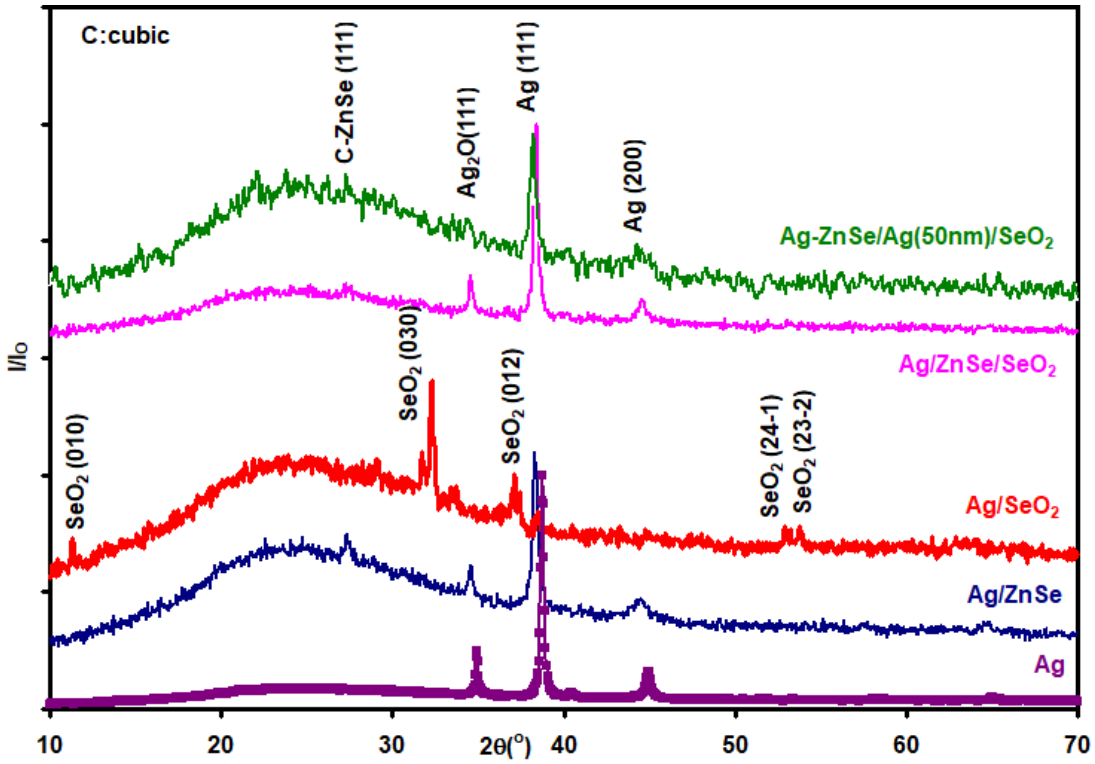

Fig. 4.1 The X-ray diffraction patterns for Ag/ZnSe , Ag/SeO_2 and Ag/ZnSe/SeO_2 Ag/ZnSe/Ag/SeO_2 heterojunction devices.

It is evident from Fig 4.1 that Ag films display three diffraction patterns at diffraction angles 34.95° , 38.75°, and 44.90°. Using 'Cristaldiff' software packages. The theoretically expected sharp patterns of face centered cubic Ag were determined. Two of the diffraction peaks centered at $2\theta = 38.75^{\circ}$ and at $2\theta = 44.90^{\circ}$ were assigned to fcc Ag being oriented along (111) and (200) directions, respectively. One peak centered at $2\theta = 38.75^{\circ}$ were not assignable to cubic Ag. This peak was indexible assuming the presence of cubic Ag_2O. Oxidation of the substrate results during the loading of the ZnSe, or SeO_2 powders into the evaporation system. The lattice parameter for cubic Ag was 4.085 Å . This phase is assigned to Fm :3m space group. For the observed Ag_2O, the lattice parameter (4.76 Å) corresponding to space group Pn-3:1. The results of the XRD analysis are compatible with the literature data for Ag [37] and for Ag_2O [38]. Fig 4.1 also illustrate XRD patterns for Ag/ZnSe thin films. In addition to the peaks of the substrate, new peak appeared at $2\theta = 27.35^{\circ}$. This peak was assigned to cubic ZnSe as reported in [39], with estimated lattice constant a of value of 5.64 Å. The observed cubic structure of ZnSe is comparable with that reported on open crystallography data base with space group F-43m of lattice constant value 5.77 Å, cubic ZnSe COD-ID: 9008857, and it is in a good agreement with literature data [39]. Coating ZnSe onto Ag make a shift in the main peak of Ag. The maximum peak of Ag is now observed at 38.4°. The calculations of the most intensive peak displays lattice parameter of 4.06 Å, and this value is closed to 4.05 Å which was previously reported [40], as well as closed to the value 4.08 Å estimated from open crystallography data base, Ag COD-ID: 1100136. As for the ZnSe/SeO_2 heterojunction, its patterns shows a four peaks with most intensive one at 38.5°. For the first peak at 26.8°, its related to cubic ZnSe. The calculated lattice constant for ZnSe is now 5.759 Å. The second peak observed at 34.75° corresponds to Ag_2O [38]

or to ZnO [41]. Preferably for Ag_2O because it was observed for the substrate peaks 38.00°. and $44.85^{\circ}$are of cubic Ag. The calculated lattice parameter of Ag is 4.048 Å that is closed to the reported value in literature data [40]. By studying the effect of introducing 50 nm Ag layer, we found no effect of Ag nanosheets on the x-ray patterns.

Fig 4.1 show the XRD patterns for the Ag/ZnSe and Ag/ZnSe/SeO_2 heterojunction comprising Ag nanosheets. The main peak and the one related to cubic ZnSe, which appears in Ag/ZnSe at $2\theta = 27.35^{\circ}$, and Ag/ZnSe/SeO_2 at $2\theta = 27.25^{\circ}$ represented mismatch of 0.36%. The analysis for the dominant most intensive peak (Ag peak) for ZnSe and ZnSe/SeO_2 indicated the crystal planes are oriented along (111) direction. The probability of appearance of Se, SeO_2, ZnO was analyzed and none of them were observed during deposition. In contrast to Ag/ZnSe/SeO_2 films, SeO_2 films coated onto Ag substrates are polycrystalline relating to the space group $P2422$ of the tetragonal phase with lattice parameters $a = 8.26$ Å and $c = 5.03$ Å. Although Ag induces the crystallization of SeO_2 when Ag is coated onto ZnSe it doesn't do the same in absence of ZnSe.

The calculated structural parameters, crystallite size (D), stacking faults (SF), defect density (δ), and micro strain (ε), for the ZnSe films coated onto Ag before and after establishing the heterojunction is shown in table 4.1.

Table 4.1 The structural parameteres of the main peak of Ag/ZnSe ,Ag/ZnSe/SeO_2 heterojunction device.

Sample	2θ	I X(10^3 c/s)	Lattice constant A° a-axis	D (nm)	ε X(10^{-3})	SF%	δ (X 10^{12} line/cm^2)
Ag/ZnSe	27.35	1.00	5.64	28.47	5.38	0.26	5.01
Ag/ZnSe/SeO_2	27.25	0.81	5.66	28.46	5.40	0.26	5.00

It is clear from the table that coating of SeO_2 onto ZnSe has increased the lattice constant from $5.64\ A^\circ$ to $5.66\ A^\circ$. The crystallite size remains unaffected. This means no enhancement in the crystallite size and no change in the micro strain and in defect density. Since the bond length of Zn-Se is $2.47 - 5.52\ A^\circ$ is larger than that of Se-O ($1.647\ A^\circ$) [42] and larger than that of Zn-O ($1.95\ A^\circ$)[43]. ZnSe has the tendency to interact with oxygen atoms of SeO_2 and with Se atom of SeO_2. The Coulomb's interaction result in bonding of some excess unbounded Zn atom and hence defect density formed by Se vacancy in ZnSe films should be reduced. It is also possible to think that since the ionic radius of O^{-2} is $140\ pm$ [44] and that of Se is $198\ pm$ [45]. Excess oxygen atoms of SeO_2 can easily fill vacant sites of Se in ZnSe and reduces the defect density, however the inability to observe these expected changes is assigned the very rough morphology of the studied films . In addition, the increase in the lattice constant upon ZnSe/SeO_2 interfacing is attributed to the difference in the ionic radii of oxygen and Se [46]. It could also be assigned to the increase in the concentration of Se as a result of coating it onto ZnSe [47].

4.2 Morphological Analysis

The scanning electron microscopy images for ZnSe substrates coated onto glass are shown in Fig 4.2 (a). The figure represents an enlargement by 20000 times of the films. It is evident from the figure that ZnSe thin films are composed of distinct nano-grains. Further enlargement by 50000 times (illustrated in the inset of Fig 4.2 (a)) show that the grains are spherical and of average size of 12 nm. Coating SeO_2 onto ZnSe dramatically changed the surface morphology of the films. As it is observable from Fig 4.2 (b) the films are composed of spherical grains of much larger sizes. At least three distinguishable classes of grains that are divided in accordance with their sizes can be found. Large grains of sizes of 1.2 μm shown by yellow circles, moderate grains of sizes of ~150 nm (shown by yellow rectangles) and small grains of sizes of ~10 nm shown by hexagons in the inset of Fig 4.2 (b). To recognize the nature of these grains the energy dispersive X-ray spectroscopy technique was employed. The results of the EDS measurements are shown in Fig. 4.2(c). The spectra show the existence of glass (SiO2:Na_2O:MgO:CaO), Zn, Se, O and Au atoms only. No other impurities were detected in the samples. The presence of Au is due to the coating of the samples to prevent electron contaminations. The EDS tests for ZnSe films revealed that the films are composed of 48.37 at. % Zn and 51.63 at. % Se. The respective chemical formula is $ZnSe_{1.07}$. The difference in the compositional stoichiometry of the ZnSe samples is less than 5.0 % of the measured value. In general, ZnSe samples contains excess selenium in its structure. On the other hand repeated measurements for the ZnSe/SeO_2 films revealed the atomic contents of ZnSe and SeO_2 in the three types of grains. However, because oxygen atoms exists in glass and in SeO_2, to monitor the composition of SeO_2, the films were coated onto Al foil. The oxygen content in the foil were tested and found to be absent. The films

coated onto Al foil revealed 32.78 at. % Se and 67.22 at.% O. The chemical formula for this samples is $SeO_{2.05}$.

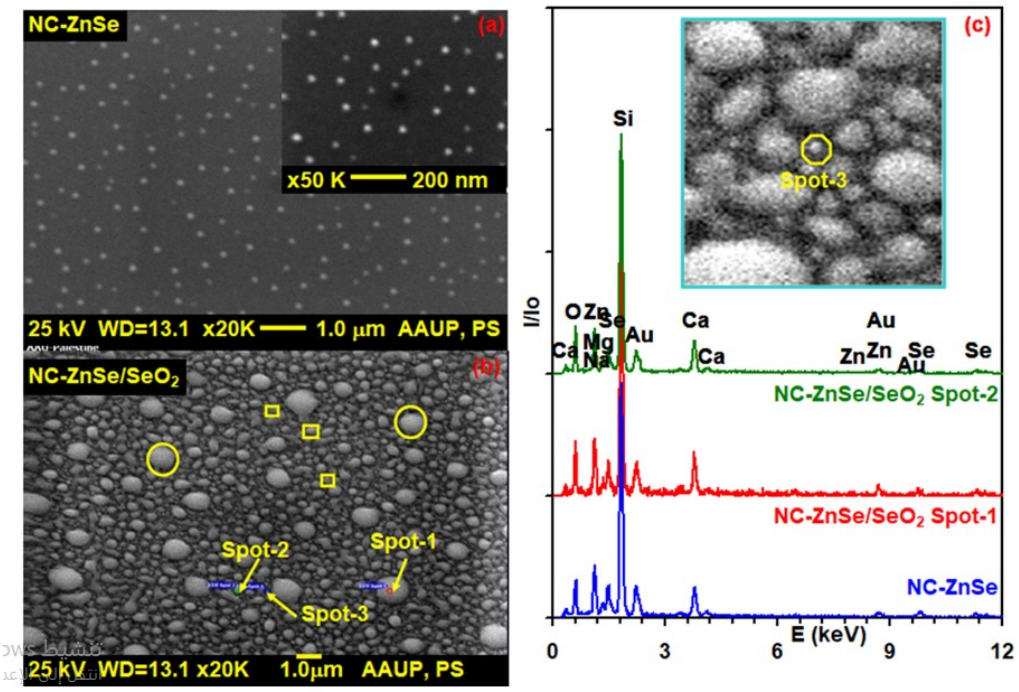

Fig 4.2. SEM images for (a) ZnSe , (b) ZnSe/SeO_2 by magnified to 20000, and (c) EDS measurements of ZnSe and ZnSe/SeO_2 films deposited on a glass slides. Inset (1) in Fig 4.2 (a) represents SEM image for ZnSe magnified to 50000.

Fig 4.3 displays the scanning electron microscopy images for the ZnSe, ZnSe/SeO_2 films coated onto Ag substrates and sandwiched with Ag nanosheets. It is evident from Fig 4.3 (a) that Ag/ZnSe films are composed of randomly distributed grains of average sizes of 120 nm. These grains are assigned to Ag substrates as the ZnSe films usually grow in sizes of 10-12 nm as were previously observed in Fig 4.2. On the other hand, when the Ag/ZnSe films are coated with SeO_2 as shown in Fig 4.3 (b) the grains follow a different distribution and exhibit three types of grains of average sizes of 500 nm (large grain shown by circles), 300 nm grains (shown by rectangles) and 90 nm (shown by hexagons). In comparison with the films coated onto glass substrates, the films coated onto Ag show that the extremely large grains (1200 nm)

decreased to 500 nm, the moderate grains which exhibited sizes of 150 nm reduced to 130 nm and the tiny grains (10 nm) disappeared instead grains of sizes of 90 appears. In addition, insertion of Ag nanosheets of 50 nm between ZnSe and SeO_2 (illustrated in Fig 4.3 (c) and (d)) resulted in very dense accumulation of grains of uniform sizes (fig 4.3 (c)) of 120 nm. When the Ag/ZnSe/Ag films are coated with SeO_2, the resulting films which are illustrated in Fig 4.3 (d) displayed grains of sizes of 200 nm in addition to those of 120 nm. However, the large size grains are randomly distributed.

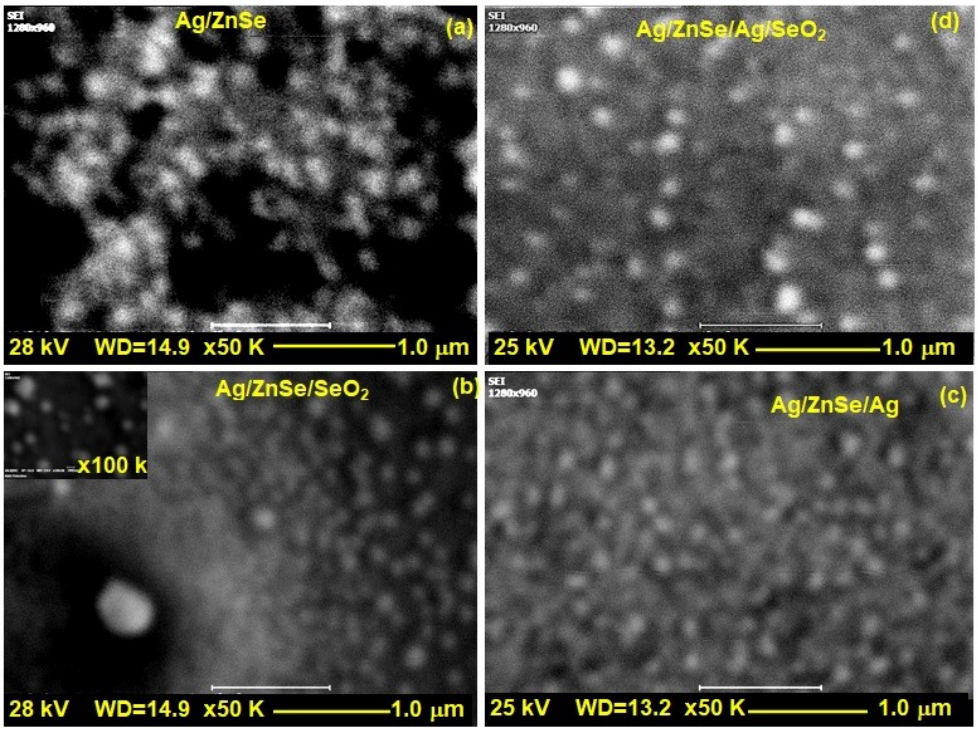

Fig 4.3. SEM images for (a) Ag/ZnSe, (b) Ag/ZnSe/SeO_2, (c) Ag/ZnSe/Ag and (d) Ag/ZnSe/Ag (50 nm)/SeO_2 thin films.

The random distribution of the grains explains the reasons beyond the inability of the XRD technique to explore the well crystallinity of the films. Recent investigations on SeO_2 films coated onto glass and Ag substrates showed that SeO_2 prefer growth in tree like clusters when coated onto Ag substrates [48]. SeO_2 films coated onto Pt substrates displayed no regular shape and are observed to be of amorphous nature

[49]. Hence it can be concluded that using Ag substrates and nanosheets significantly improves the morphology of the films.

4.3 Construction of the Energy Band Diagram

The energy band diagram is prepared based on the knowledge of the energy band gap. For this reason we have measured the optical transmittance and reflectance and calculated the absorption coefficient (α). With a view to determine the energy band diagram of ZnSe/SeO_2 heterojunction devices, we were directed to determine the energy band gap of the ZnSe and SeO_2 individually. So that the optical properties of the ZnSe and SeO_2 have been measured and the absorption coefficient is determined.

The transmittance and reflectance of the ZnSe and SeO_2 were presented in Fig 4.4 , respectively.

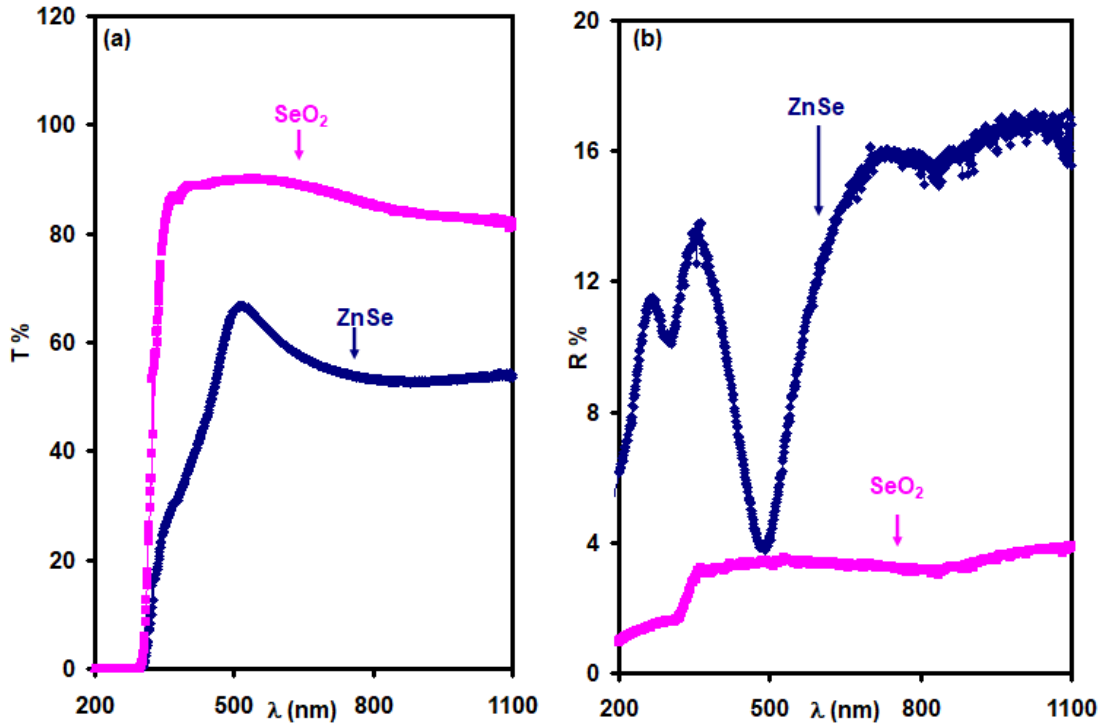

Fig 4.4 The optical (a) transmittance and (b) reflectance for ZnSe , SeO_2 thin films.

Plotting Tauc's equation [50] allowed us finding the energy band gap of ZnSe is indirect band gap as 2.78 eV . The E-axis crossing is shown in Fig 4.5 (a). In the same manner the energy band gap of SeO_2 is direct and determined to be 3.69 eV as from E-axis crossing shown in Fig 4.5 (b).

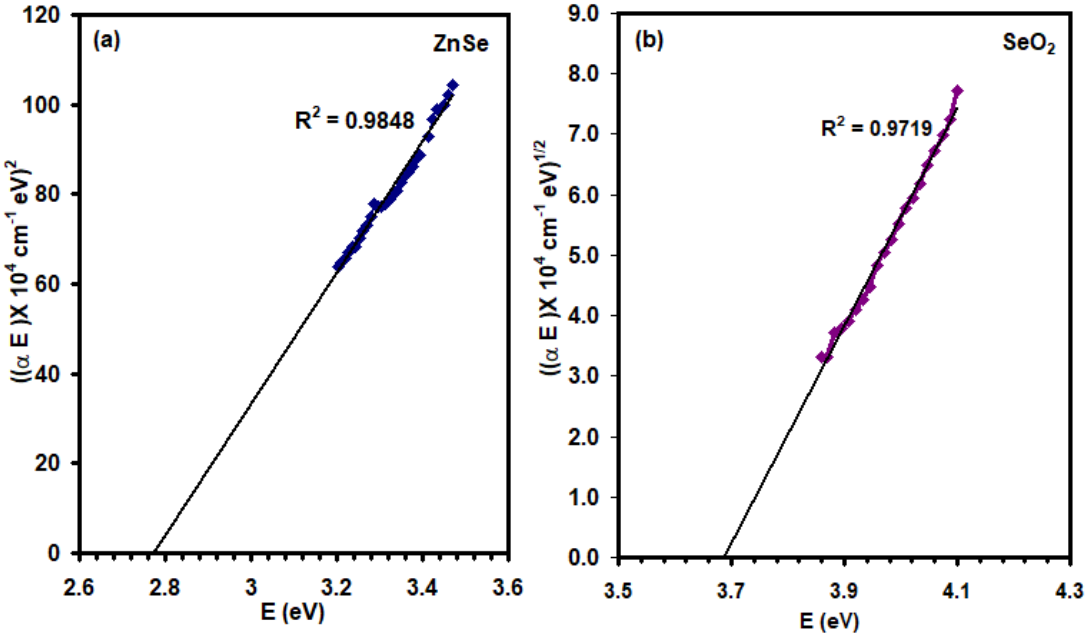

Fig. 4.5 (a) The $(\alpha E)^2$ – E for ZnSe , (b) The $(\alpha E)^{1/2}$ –E for SeO_2.

As indicated in literature data, the electron affinity ($q\chi$) and work function values are of 3.80 $eV$and 4.81 eV for the ZnSe [51] . For SeO_2, electron affinity was estimated from the enthalpy of formation which show value of 1.89 eV [52]. The work function for SeO_2 was estimated experimentally, Fig 4.6 represents the Arrhenius plot of electrical resistivity (ρ) - temperature (T) variations for the glass/SeO_2 sample, the resistivity was measured at temperature range 291-417 K. The slope of the curve Ln (ρ) - T^{-1} follow the Arrhenius equation $\rho(T) \propto exp^{\left(E_a/KT\right)}$ [53] indicates a resistivity activation energy (E_a) of 0.379 eV for SeO_2 sample. This value of activation energy is

less than the value of half the energy band gap 3.69 eV. Since the activation energy represent the acceptor level in SeO_2, the Fermi level should lay at mid distance between E_a and valence band. Hence the work function is

$$q\varphi = q\chi + E_g - \frac{|E_V - E_F|}{2}$$

$$q\varphi = 1.89 + 3.69 - \frac{0.379}{2}$$

$$q\varphi = 5.40\ eV$$

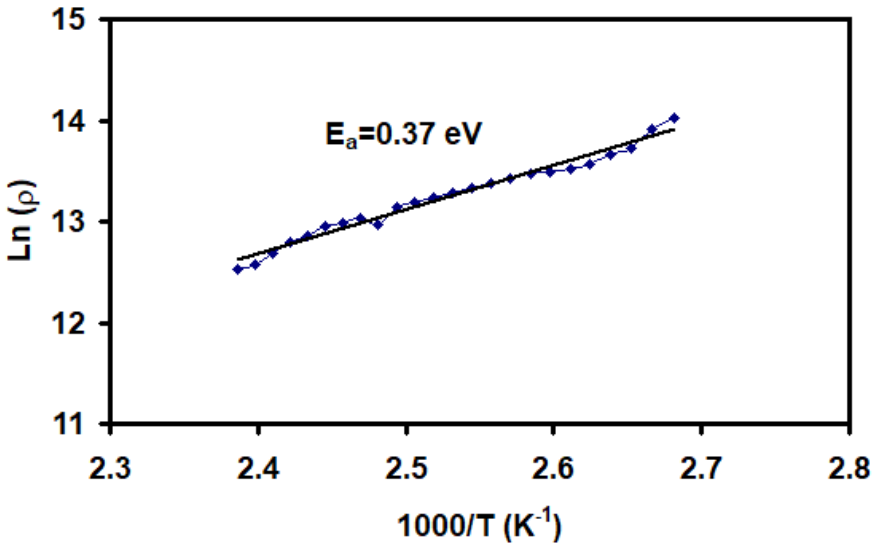

Fig. 4.6 the logarithmic plots of electrical resistivity for the SeO_2.

Based on the mentioned values, the value of the conduction ($\Delta E_c = |q\chi_{ZnSe} - q\chi_{SeO_2}|$) and valence ($\Delta E_v = |\Delta E_c - \Delta E_g|$) offsets are determined to be 1.91 eV and 0.91 eV, respectively. These values are large enough to actualize quantum confinement which is necessary for fabricating thin film transistors [54]. Using hot probe technique, we find the type of conduction for ZnSe it is n-type, and for SeO_2 is p-type. Thus they construct p-n heterojunction, with the value of the build in voltage ($qV_{bi} = |\phi_{ZnSe} - \phi_{SeO_2}|$ of 0.59 eV. On the other hand, the Carbon metal exhibits

work function of 5.10 *eV* [55], which is larger than that of ZnSe indicating the formation of a schottcky contact. As for SeO_2, C/SeO_2 pointing to an ohmic nature of contact. Hence the device under study represent p-n junction connected to one schottcky arm. Energy band diagram before contact represented in fig 4.7, while energy band diagram after contact represented in fig 4.8.

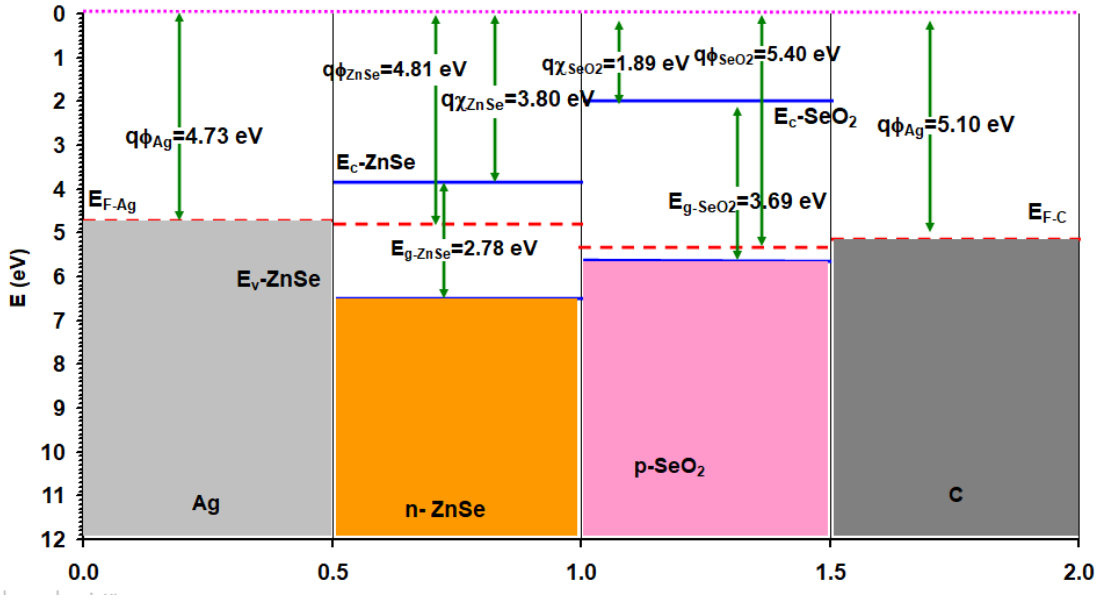

Fig. 4.7 The flat energy band diagram for Ag/ZnSe/SeO_2/C heterojunction

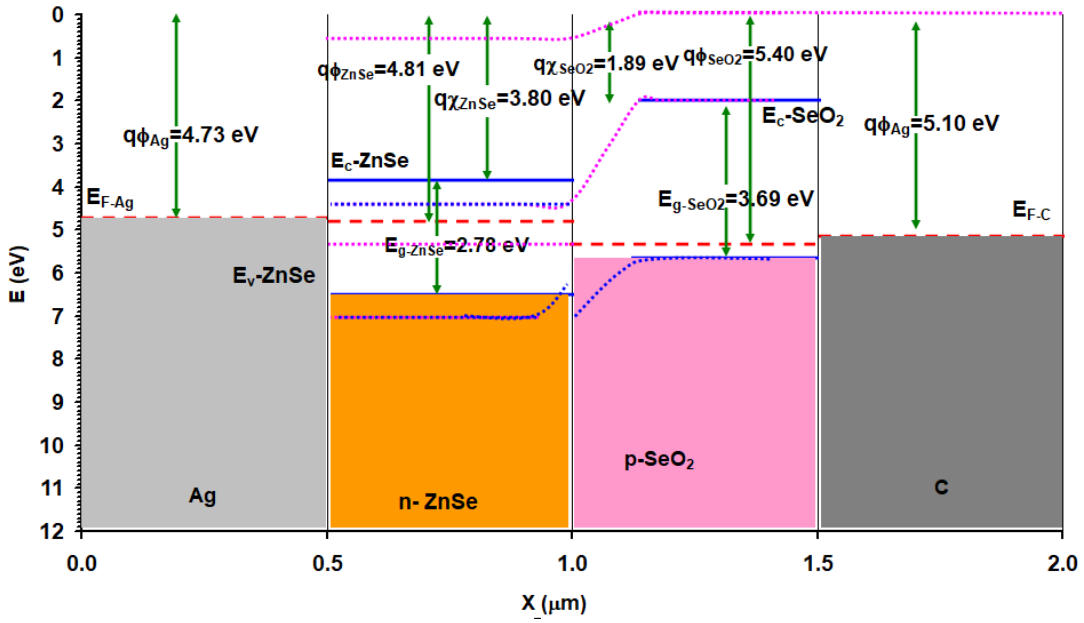

Fig. 4.8 The energy band diagram after contact for Ag/ZnSe/SeO_2/C heterojunction.

4.4 Impedance Spectroscopy Analysis

To find out applications for the ZnSe/SeO_2 heterojunction devices, the electrical performance was studied and analyzed by impedance spectroscopy technique in the frequency domain 1-1800 MHz. For this purpose Agilent 4291B 0.01-1.80 GHz is used as an impedance analyzer. The ZnSe/SeO_2 was deposited on silver (Ag) substrate and circular point of carbon of area of $3.14 \times 10^{-2}\ cm^2$ was painted on the top of the heterojunction to complete the connection for analyzing. When the device was placed between both terminals of the impedance analyzer, an ac signal was passed through the electrodes of the device. Fig 4.9 show the spectra of capacitance of the resulting ac signal, respectively. Analyzing of capacitance was done for series type of conduction.

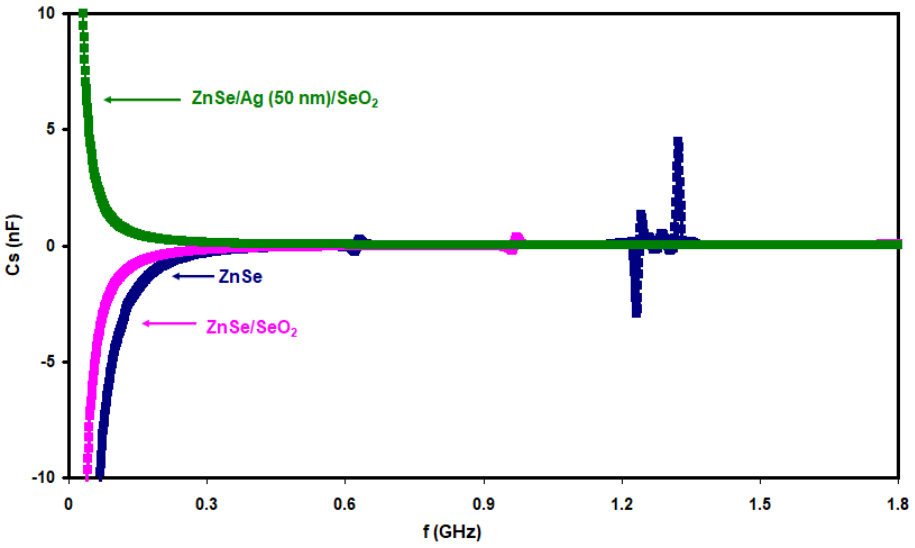

Fig. 4.9 The capacitance spectra for the Ag/ZnSe/C, Ag/ZnSe/SeO_2/C and Ag/ZnSe/Ag (50 nm)/SeO_2/C heterojunction devices.

The capacitance spectra for Ag/ZnSe/C are shown in Fig 4.10. It represents a negative capacitance effect in the low frequency range. The capacitance increases with

increasing frequency until 0.6 GHz is reached, at 0.6 GHz, the capacitance decreased very sharply showing an anti resonance of negative capacitance of value 0.25 nF, and a resonance of capacitance of value 0.63 nF. In addition, another anti resonance-resonance peak appears at a frequency of 1.23 GHz with capacitance value of -2.95 nF and resonance at 1.24 GHz with 1.36 nF capacitance. There was a resonance another 1.32 GHz of capacitance of value of 4.48 nF . On the other hand, after coating Ag/ZnSe with SeO_2 layer to form the heterojunction, a variation in the capacitance spectra occurs. Fig 4.11 for Ag/ZnSe/SeO_2/C shows a negative capacitance in the frequency range below 1.00 GHz, negative capacitance of value of 0.19 nF., that is the capacitance exhibit anti resonance - resonance phenomena at 0.96 GHz and 0.97 GHz, respectively. For Ag/ZnSe/Ag (50nm)/SeO_2/C , Fig 4.12 represents a decreasing trend in the capacitance spectra which is limited in the positive range of frequency values.

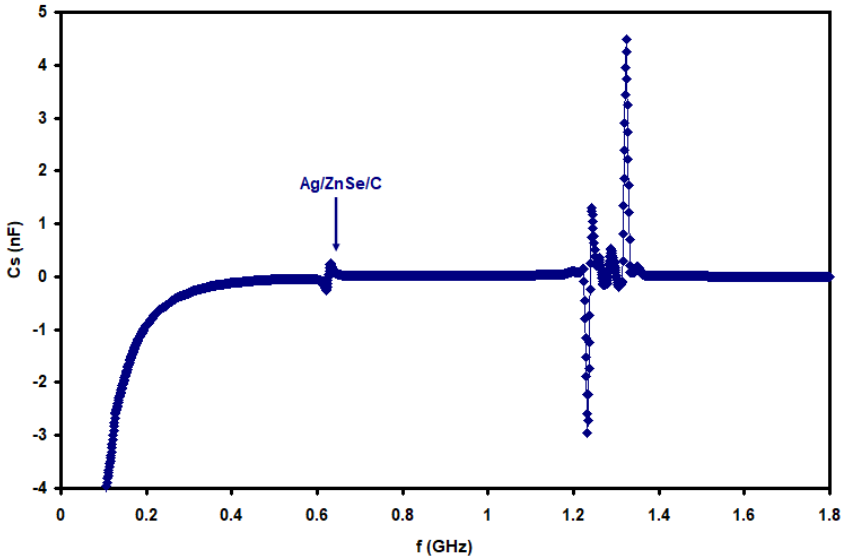

Fig 4.10 The capacitance spectra for the Ag/ZnSe/C

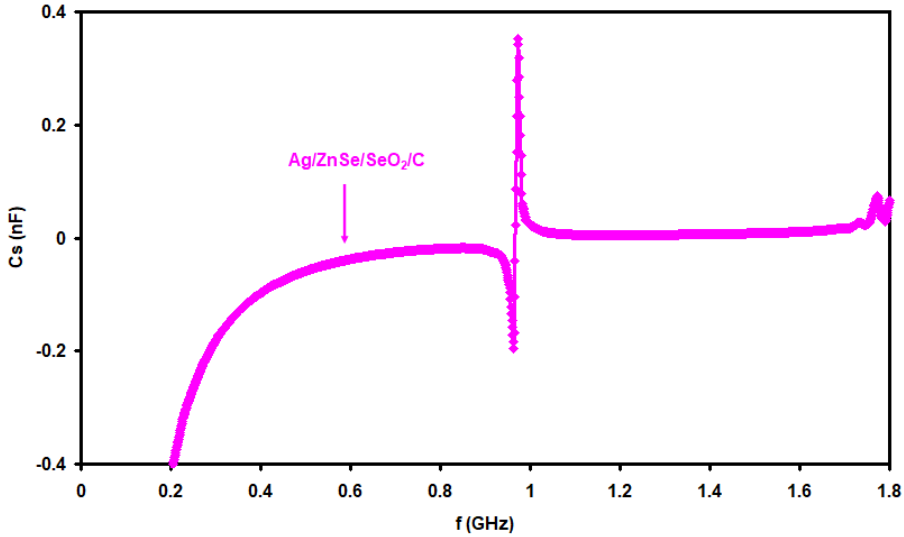

Fig 4.11 The capacitance spectra for the Ag/ZnSe/SeO_2/C

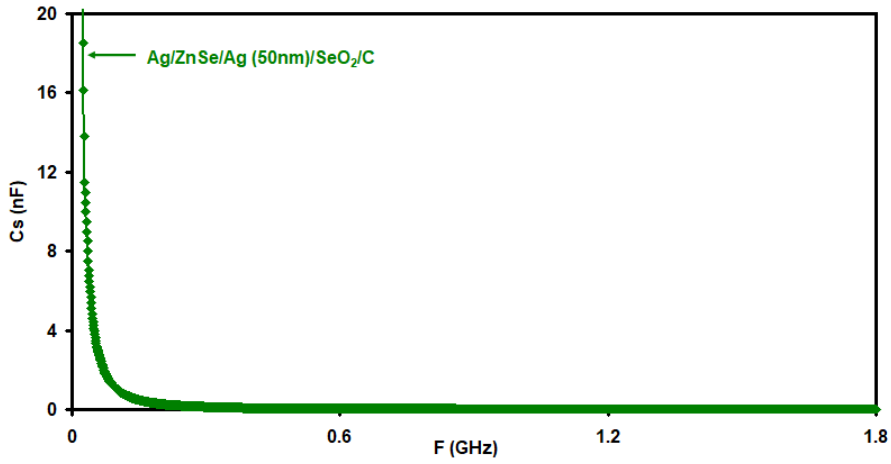

Fig 4.12 The capacitance spectra for the Ag/ZnSe/Ag (50 nm)/SeO_2/C

In order to explain the behavior of the capacitance with frequency, resonance – anti resonance, negative capacitance, the physical changes in capacitance spectra of Ag/ZnSe/C, Ag/ZnSe/SeO_2/C and Ag/ZnSe/Ag (50 nm)/SeO_2/C, they were modeled by Qasrawi-Ershov model. The experimental information obtained was reformulated according to equation (2.25), and was shown in figures 4.13 ,4.14, 4.15, for Ag/ZnSe/C, Ag/ZnSe/SeO_2/C and Ag/ZnSe/Ag (50 nm)/SeO_2/C, respectively.

The spectra that expresses the theoretical solution were plotted by the black line , it is observed that there is accepted compatibility between theoretical and experimental data. The parameters which make that fitting are consistent with experiment is shown in table (4.2). The first thing can be taken into account is the obvious change in geometrical capacitance, in which the geometrical capacitance increased from 16 pf to 66 pF when SeO_2 was evaporated onto ZnSe .

As it is observed from Fig 4.13, the capacitance of ZnSe is negative in the range 0.01-0.50 GHz. This phenomenon needs a_1 of equation (2.25) to be zero, where a_2= 3.00 F/s , with limiting radial frequency ω_2 of 0.08 GHz, The spectra of capacitance display two anti resonance-resonance, one at 0.64 GHz (below 1.00 GHz), the other at 1.24 GHz (above 1.00 GHz). The spectra of capacitance is reproduced by taking the values of pre-exponential parameters a_1 and a_2 to be 1.00 F/s for the two anti resonance-resonance regions, and values of limiting radial frequency (ω_1,ω_2) to be (3.94, 3.94) GHz, for the region below 1.00 GHz, and (7.78 , 7.75) GHz for the region above 1.00 GHz. Above that limit (1.00 GHz), there is a resonance reproduced with value of a_1=1.00 F/s (where a_2=0.00), and ω_2 is 7.75 GHz . The theoretical solution that fits the experimental data considering the whole studied range of frequency is represented in fig 4.13 (a), (b), and (c) .

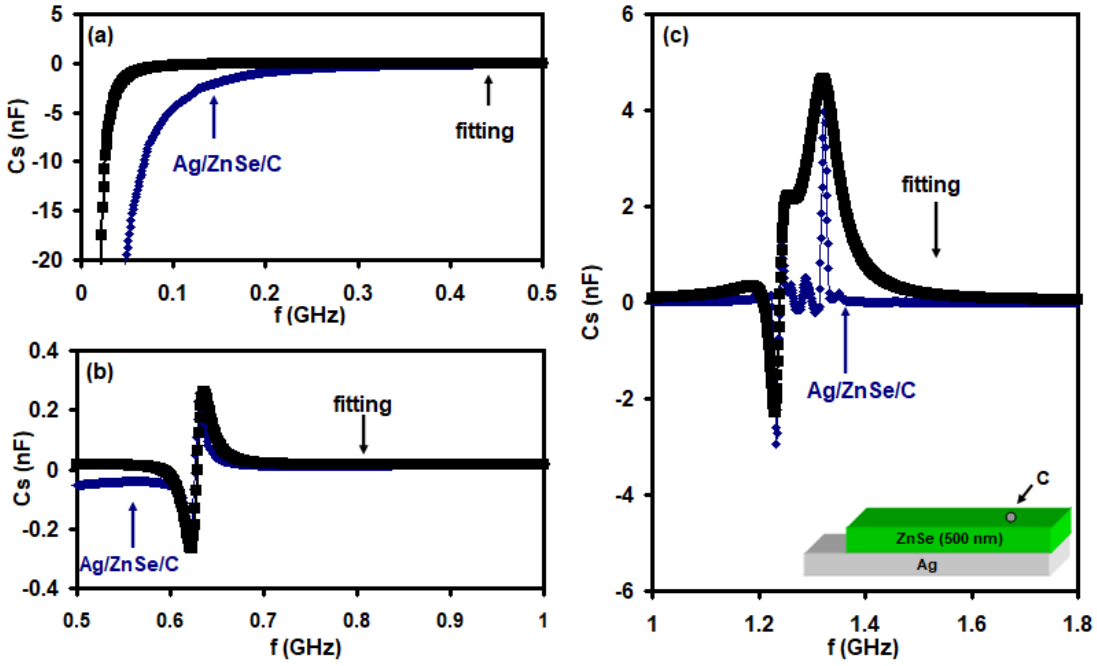

Fig. 4.13 The modeled curve of the capacitance spectra for Ag/ZnSe/C, (a) frequency range 0.0-0.5 GHz , (b) frequency range 0.5-1.0 GHz , (c) frequency range 1.0-1.8 GHz. The black lines represent the fitting.

On the other hand, Fig 4.14 displays the capacitance spectra of Ag/ZnSe/SeO_2/C, which indicates a negative capacitance effect in the frequency domain of 0.01-1.00 GHz , Fig 4.14 (a) that request no positive part (a_1=0.00), with anti resonance part with a_2=3.00, and limiting radial frequency ω_2=0.08 GHz. For frequency above 1.00 GHz, Fig 4.14 (b) exhibits anti resonance-resonance capacitance effect. The parameters needed for fitting were a_1=1.00 F/s, a_2= 1.00 F/s, ω_1=6.16 GHz and ω_2= 6.15 GHz. The capacitance for the two regions represents the theoretically reproduced experimental data for Ag/ZnSe/SeO_2/C as seen in fig 4.14 (a) and (b).

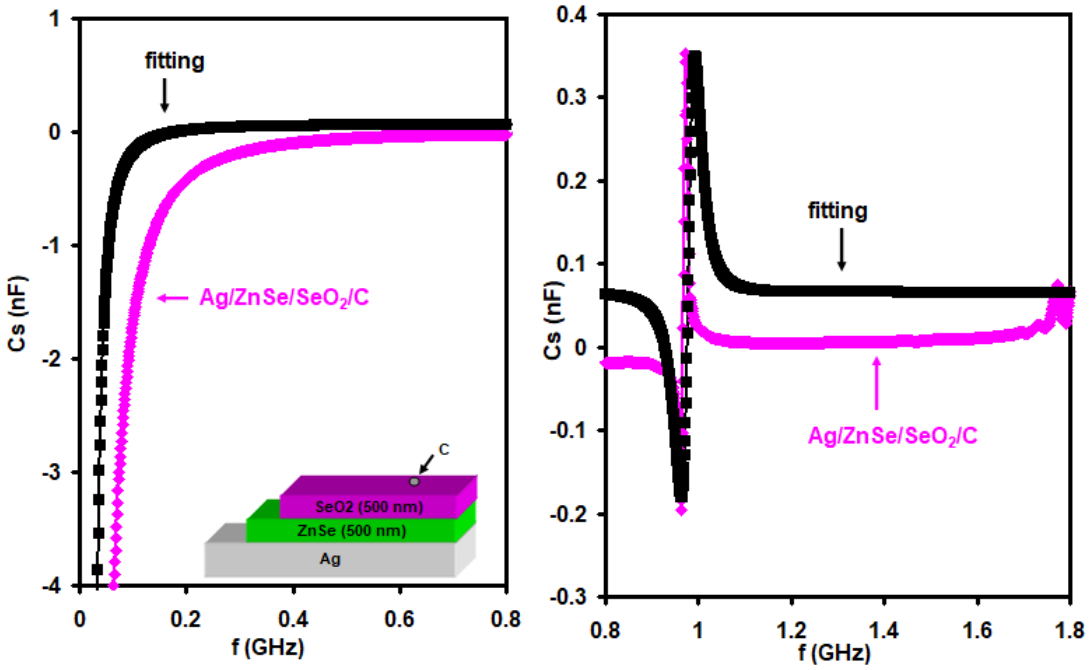

Fig. 4.14 The modeled curve of the capacitance spectra for Ag/ZnSe/SeO_2/C, (a) frequency range 0.0-0.8 GHz , (b) frequency range 0.8-1.8 GHz . The black lines represent the fitting.

In addition, for Ag/ZnSe/Ag (50 nm)/SeO_2/C , the capacitance exhibit a positive values for the whole range of frequency , the capacitance spectra decreases until reaching 1.80 GHz as shown in Fig 4.15. The data is reproduced assuming fitting parameters a_1=3.00 F/s (where a_2=0.00) , and $\omega_1 = 0.05$ GHz. It is clear that the Ag nanosheets have significantly altered the charge dynamics at the interface. Recalling that negative capacitance effect always resulted from charge instabilities at the ZnSe/SeO_2 interface. The presence of Ag as a free e^- source and as a bond complement successfully removed the negative capacitance effect.

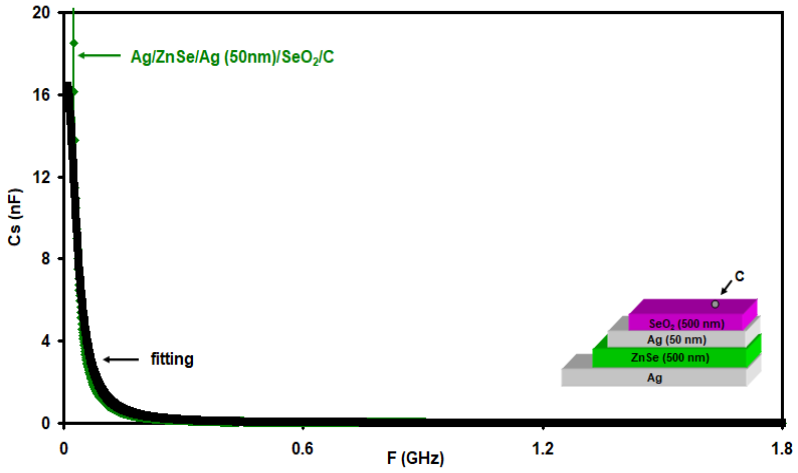

Fig. 4.15 The modeled curve of the capacitance spectra for Ag/ZnSe/Ag (50 nm)/SeO_2/C.

Fig 4.16 presents the spectra of conductivity for Ag/ZnSe/C, Ag/ZnSe/SeO_2/C, and Ag/ZnSe/Ag (50nm)/SeO_2/C. In this figure, the variations in conductivity with frequency are shown . The observations for Ag/ZnSe/C conductivity spectra indicate a decreasing trend in conductivity reaching a minima at 0.75 GHz, in the frequency domain of 0.75 – 1.12 GHz. The conductivity increases showing peak at 1.12 GHz. Above this frequency, the conductivity decreases. The conductivity of Ag/ZnSe/SeO_2/C as seen from the figure decreasing with increasing frequency until 1.50 GHz is reached, then increases and display a peak at 1.77 GHz. In the remaining range of frequency the conductivity decreases. For Ag/ZnSe/Ag (50 nm)/SeO_2/C, the conductivity decreases in whole range of frequency.

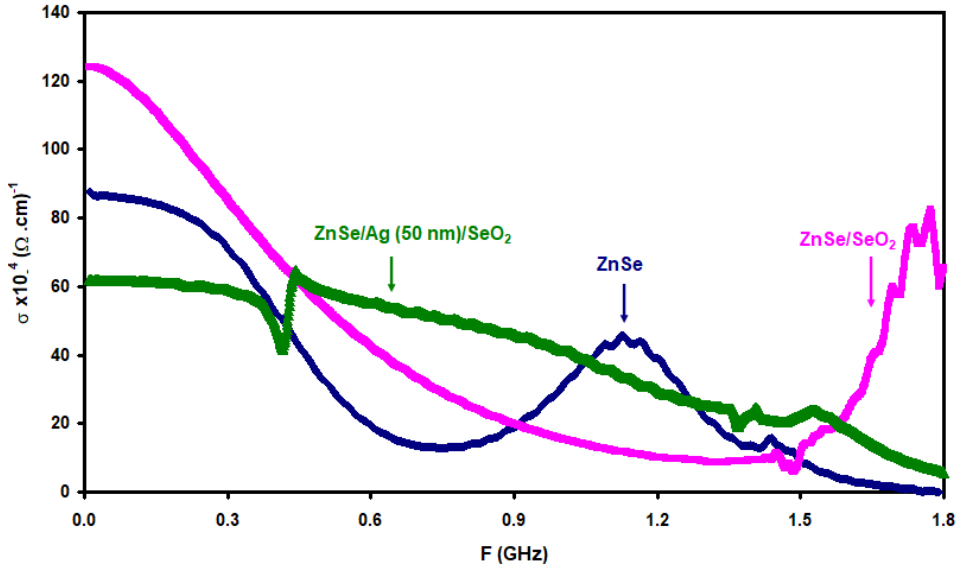

Fig 4.16 The conductivity spectra for the Ag/ZnSe/C, Ag/ZnSe/SeO_2/C and Ag/ZnSe/Ag (50 nm)/SeO_2/C heterojunction devices.

To explore the physics laying beyond the behavior of the conductivity spectra, theoretical models were taken into account. One of these models which describe the current conduction mechanism in the conductivity spectra is the correlated barrier hopping (CBH) and the quantum mechanical tunneling (QMT). The theories which explain how to deal with these mechanisms are shown in chapter two of this thesis. As shown in fig 4.16, The correlated barrier hopping dominated below 1.50 GHz, the quantum mechanical tunneling dominated above 1.50 GHz. In Ag/ZnSe/C, Ag/ZnSe/SeO_2/C, it clearly shows that each of them has (CBH) and (QMT), on other hand, (CBH) dominated in larger frequency values Ag/ZnSe/SeO_2/C than in Ag/ZnSe/C. For Ag/ZnSe/Ag (50 nm)/SeO_2/C, (CBH) dominated.

Modeling and fitting of experimental data was possible for the electrical conductivity of the three channels named Ag/ZnSe/C, Ag/ZnSe/SeO_2/C and Ag/ZnSe/Ag (50 nm)/SeO_2/C. The fitting done using equation (2.18) and shown in figure 4.17 helps extracting the fitting parameters of ac conductivity. The fitting parameters are tabulated in Table 4.2. As it is clear from Fig 4.17 (a) and (b), the

electronic conduction for the two channels contains correlated barrier hopping and quantum mechanical tunneling in the studied frequency domain, with stronger domination of correlated barrier hopping through Ag/ZnSe/SeO_2/C channels than Ag/ZnSe/C channels. Factors that are affecting this compatibility between experimental and theoretical data are the values of high-frequency and low-frequency conductivity $(\sigma(H), \sigma(L))$ which were 8.7×10^{-3}, 8.9×10^{-3},and 1.0×10^{-4}, $1.24 \times 10^{-2}\ (\Omega\ cm)^{-1}$ for Ag/ZnSe/C and Ag/ZnSe/SeO_2/C, respectively (see table 4.2). Fig 4.17 (a) and (b) for Ag/ZnSe/SeO_2/C, displays theoretically calculated $\sigma_{CBH}(\omega)$ which is dominant in the range below 0.75 GHz, and $\sigma_{Tunneling}(\omega)$ which is dominated for frequencies above 0.75 GHz. As mentioned in the table 4.2, the relaxation time parameter reveals a value of 10 ns for Ag/ZnSe/C and 3 ns for Ag/ZnSe/SeO_2/C for the whole proposed range of frequency. In addition, the density of localized states at the Fermi level for Ag/ZnSe/SeO_2/C is $N(E_F) = 4.5 \times 10^{20}\ cm^{-3}\ eV$ which is higher when compared to its value for Ag/ZnSe/C of $2.0 \times 10^{20}\ cm^{-3}\ eV$. Fig 4.17 (c) displays theoretically calculated $\sigma_{CBH}(\omega)$ which is dominated in the whole range of frequency for Ag/ZnSe/Ag (50 nm)/SeO_2/C channels. The values of high-frequency and low-frequency conductivity $(\sigma(H), \sigma(L))$ were $(10.00 \times 10^{-6}, 0.62 \times 10^{-2})\ (\Omega\ cm)^{-1}$, respectively. As mentioned in the table 4.2, the relaxation time parameter exhibits a value of 10 ps.

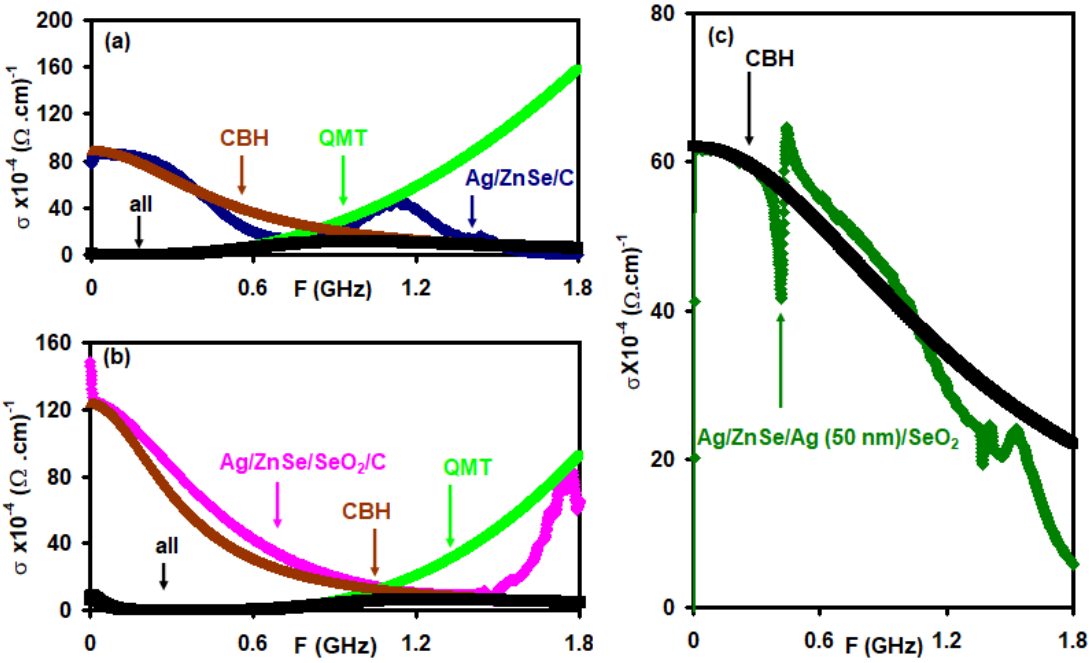

Fig. 4.17 The modeled curve of the conductivity spectra for (a) Ag/ZnSe/C, (b) Ag/ZnSe/SeO_2/C, and (c) Ag/ZnSe/Ag (50 nm)/SeO_2/C heterojunction devices. The black lines represent the fitting

Table 4.2 The electrical conduction parameteres for Ag/ZnSe/C, Ag/ZnSe/SeO_2/C and Ag/ZnSe/Ag (50 nm)/SeO_2/C heterojunction devices.

Parameter	Ag/ZnSe/C				Ag/ZnSe/SeO_2/C		Ag/ZnSe/Ag (50 nm)/SeO_2/C
	(f<0.50) GHz	(0.50 <f<1.00) GHz	(1.00 <f<1.25)GHz	(1.25<f)GHz	(f<0.50) GHz	(0.50 <f<1.50) GHz	(f<1.80) GHz
τ_0 (ns)	10.00	10.00	10.00	10.00	3.00	3.00	0.01
τ_{hop} (ns)	2.00	2.00	2.00	2.00	2.93	2.93	0.75
$N(E_F)$ (x10^{20} $cm^{-3}eV$)	2.00	2.00	2.00	2.00	4.50	4.50	___
σ(L) x (10^{-2} $\Omega^{-1}cm^{-1}$)	0.89	0.89	0.89	0.89	1.24	1.24	0.62
σ(H) x (10^{-4} $\Omega^{-1}cm^{-1}$)	87.00	87.00	87.00	87.00	1.00	1.00	0.10
C_o (pF)	16.00	16.00	16.00	16.00	66.00	66.00	0.60
a_1	___	1.00	1.00	1.00	___	1.00	3.00
a_2	3.00	1.00	1.00	___	3.00	1.00	___
w_{pe1} (GHz))	___	3.94	7.78	8.30	___	6.16	0.05
w_{pe2} (GHz)	0.08	3.94	7.75	___	0.08	6.15	___

In addition, the impedance spectra for Ag/ZnSe/C, Ag/ZnSe/SeO_2/C and Ag/ZnSe/Ag(50 nm)/SeO_2/C heterojunction devices were investigated. Fig 4.18 (a) displays the impedance spectra, for Ag/ZnSe/C. It appears that the impedance is increasing in small rate with increasing signal frequency in range of 0.00-0.40 GHz. Then it increases at higher until it reaches a peak at 0.68 GHz. It decreased with frequency until it reaches minima at 1.20 GHz. After that point, the impedance increased sharply to have a maximum value at 1.73 GHz. For Ag/ZnSe/SeO_2, its spectra shows an increasing trend in impedance with increasing signal frequency until reaching a peak at 1.05 GHz, then impedance decreased in frequency domain of 1.05-1.80 GHz. For the third sample Ag/ZnSe/Ag(50 nm)/SeO_2/C, impedance exhibits a one local peak, one local minima at 0.40 GHz, and 0.44 GHz ,respectively. High impedance indicates low amount of current that passes per unit voltage, while low impedance means more current can pass through device per unit voltage. The conduction mechanism at the interface controlled the impedance variations .On the other hand, the reflection coefficient ρ assured the variations in impedance spectra which was calculated according to the relation $\rho = \frac{Z_{Device} - Z_{Source}}{Z_{Device} + Z_{Source}}$, and displayed in fig 4.18 (b). Reflection coefficient represents the quality of the impedance matchs between the source and the measured devices. Lower value of ρ indicates better matches. The ρ values range from -1 for shorts, zero for best matches, and could reach +1 for open loads. The figure shows that reflection coefficient remains constant in frequency domains 0.00-0.40 GHz and 0.80-1.10 GHz. It also exhibits two absolute minima at 0.65 GHz of 0.26, and 1.50 GHz of 0.08 for Ag/ZnSe/C device. Also, its clear from fig 4.18 (b) that Ag/ZnSe/SeO_2/C exhibits one absolute minima at 1.00 GHz of 0.13. On the other hand, for the heterojunction contain Ag in between,

reflection coefficient exhibit two peaks, local minima and local maxima at 0.39 GHz and 0.43 GHz, respectively.

In addition, the return loss which is a measure of unabsorbed power by the device and is returned to the source, is also evaluated. Absolute values of return loss larger than 20 dB indicates excellent band pass/stop filters characteristics [56]. For the three devices, as shown in fig 4.18 (c), there is one position satisfying the condition Lr ≥ 20dB, it is in the frequency domain 1.49-1.51 GHz in the spectra of Ag/ZnSe/C. This feature indicated that the designed band filters are ideal for 4G/5G communication technology.

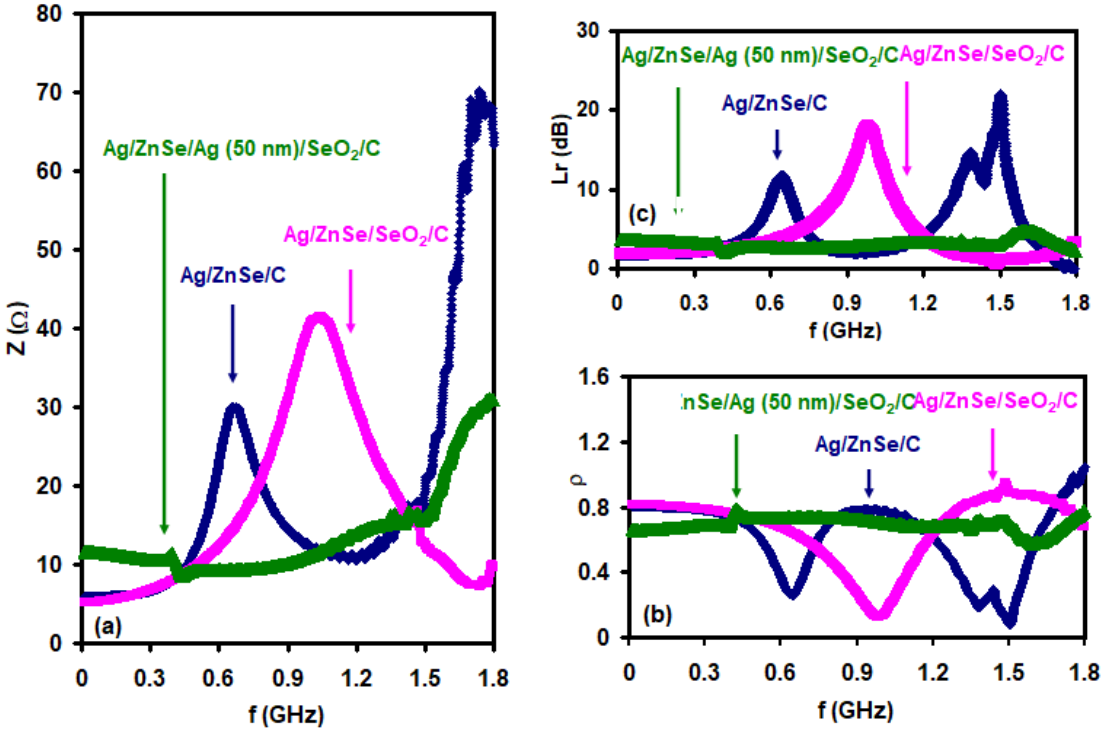

Fig.4.18 The (a) impedance, (b) reflection coefficient and (c) return loss spectra of Ag/ZnSe/C, Ag/ZnSe/SeO_2/C and Ag/ZnSe/Ag(50 nm)/SeO_2/C heterojunction devices.

4.5 Current-Voltage Characteristics

To see the performance of the ZnSe, ZnSe/SeO_2 heterojunction, ZnSe/Ag (50 nm)/SeO_2 devices, current (I)- voltage (V) measurements were carried out. The three samples were deposited onto Ag substrate, each sample painted by carbon as a point contact, I-V measurements for the proposed samples were recorded in the dark. The measured I-V characteristics were shown in Fig 4.19. As the conductivity type was determined for ZnSe (n-type),for SeO_2 (p-type), so ZnSe/SeO_2 displayed p-n heterojunction . The type of contact estimated from the analysis of I-V measurements was ohmic contact for the three proposed samples. One possible reason is the roughness of the film surface as we have observed in the scanning electron microscopy images. Another reason, is the diffusion of carbon and silver metallic atoms in vacant sites of ZnSe and SeO_2 respectively. The third reason could be the large defect density in the films.

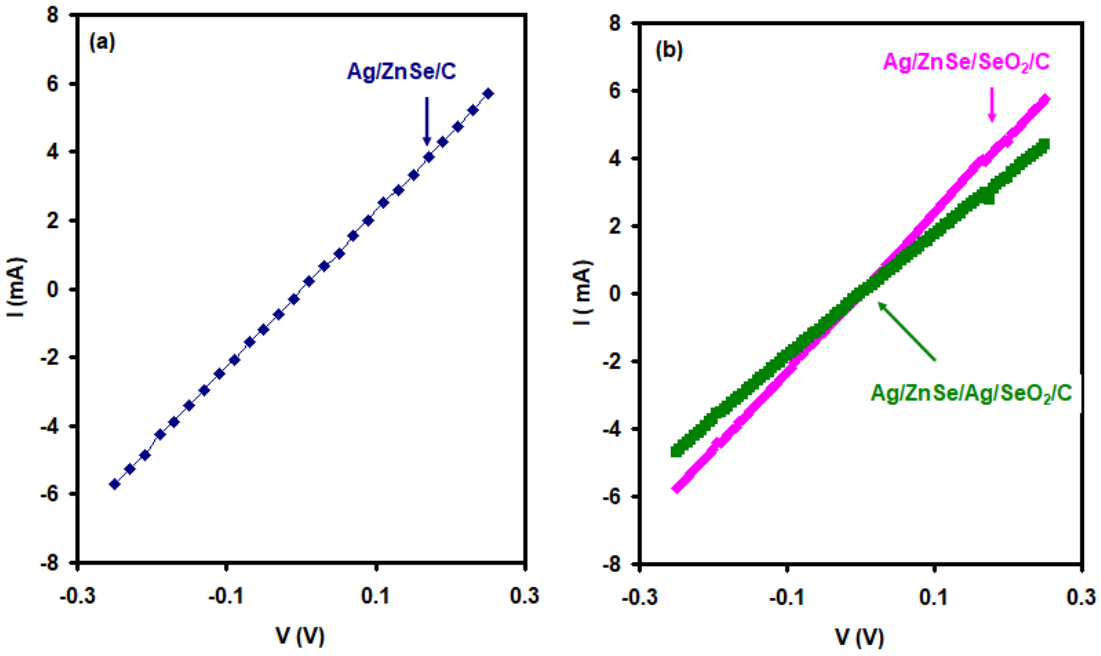

Fig. 4.19 The current-voltage characteristics , (a) for Ag/ZnSe/C, (b) for Ag/ZnSe/SeO_2/C and Ag/ZnSe/Ag(50 nm)/SeO_2/C heterojunction devices.

Chapter Five

Conclusions

In the current study we have focused on exploring the structural, morphological and electrical properties of stacked layers of ZnSe and SeO_2 in thin film forms. The proposed heterojunction devices exhibited polymorphic structure and showed valence and conduction band offsets that allow then for use as thin film transistors. The sketch of the energy band diagram of the device have shown a built in potential of $0.61\ eV$. The work function of SeO_2 is also experimentally determined and found to be $5.40\ eV$. In addition, the impedance spectroscopy studies on the ZnSe/SeO_2 interfaces have shown it is suitability to use as negative capacitance thin film transistors and as microwave resonators. The devices showed enhanced resonance-antiresonance phenomena at $\sim 1.0\ GHz$. Such property assure the possibility of using the device as microwave resonator. Moreover, deep analysis of the conductance spectra in the frequency domain $0.01 - 1.80\ GHz$ have shown that the current conduction in the ZnSe/SeO_2 ac signal filters is dominated by the correlated barrier hopping and by the quantum mechanical tunneling. Furthermore, modeling the capacitance spectra indicating that surface charge injection leading to the negative capacitance effect. In addition to these features ZnSe/SeO_2 devices showed wide band stop filter characteristics nominating them for use as microwave band filters.

References:

[1] Suthar, D., Chasta, G., Patel, S. L., Chander, S., Kannan, M. D., & Dhaka, M. S. (2020). Impact of different annealing conditions on physical properties of ZnSe thin films for ecofriendly buffer layer applications. Materials Research Bulletin, 132, 110982.

[2] Sharma, Y. C., Ansari, P., Sharma, R., Mathur, D., & Dar, R. A. (2021). Bandgap tuning of optical and electrical properties of zinc selenide. *Chalcogenide Letters*, *18*(4), 183-189.

[3] Yuan, Y., Liu, C., Li, Y., & Li, J. (2021). Influence of Annealing Temperature Modulation on the Structural and Optical Properties of ZnSe Thin Films. *Crystal Research and Technology*, *56*(5), 2000177.

[4] Hendrickson, A. T. (2020). *Synthesis and Design of Zinc Selenide and Multi-Material Optical Fibers for High Power Mid-Infrared Applications*. The Pennsylvania State University.

[5] Lee, S. H., Song, S. W., Yoon, S. Y., Jo, D. Y., Kim, S. K., Kim, H. M., ... & Yang, H. (2021). Heterostructural tailoring of blue ZnSeTe quantum dots toward high-color purity and high-efficiency electroluminescence. *Chemical Engineering Journal*, 132464.

[6] Ke, J., Zhang, R., Zhang, P., Yu, R., Cao, X., Kuang, P., & Wang, B. (2021). Investigation on structural and optical properties of ZnSe thin films prepared by selenization. *Superlattices and Microstructures*, 106965.

[7] Khalfi, R., Talantikite-Touati, D., Tounsi, A., & Merzouk, H. (2020). Effect of deposition time on structural and optical properties of ZnSe thin films grown by CBD method. *Optical Materials*, *106*, 109989.

[8] Chuhadiya, S., Sharma, R., Patel, S. L., Chander, S., Kannan, M. D., & Dhaka, M. S. (2020). Thermal annealing induced physical properties of ZnSe thin films for buffer layer in solar cells. *Physica E: Low-dimensional Systems and Nanostructures*, *117*, 113845.

[9] Ion, L., Iftimie, S., Radu, A., Antohe, V. A., Toma, O., & Antohe, S. (2021). Physical properties of RF-sputtered ZnSe thin films for photovoltaic applications: Influence of film thickness. *Porc. Rom. Acad. Ser. A*, *22*, 25-34.

[10] Hasaneen, M. F., Alrowaili, Z. A., & Mohamed, W. S. (2020). Structure and optical properties of polycrystalline ZnSe thin films: validity of Swanepol's approach for calculating the optical parameters. *Materials Research Express*, *7*(1), 016422.

[11] Hile, D. D., Swart, H. C., Motloung, S. V., Kroon, R. E., Egbo, K. O., & Koao, L. F. (2020). The effect of annealing time on zinc selenide thin films deposited by photo-assisted chemical bath deposition. *Journal of Physics and Chemistry of Solids*, *140*, 109381.

[12] Ou, K., Wang, S., Bai, L., Wang, Y., Zhang, K., & Yi, L. (2019). Investigation on annealing temperature-dependent optical properties of electron beam evaporated ZnSe thin films. *Thin Solid Films*, *669*, 247-252.

[13] Abed, H., Alsultani, M., Abdulsattar, M., & Abduljalil, H. (2020). Structural and Vibrational Properties of ZnSe Nanostructures: A DFT/TDDFT Study. *Egyptian Journal of Chemistry*, *63*(6), 2009-2018.

[14] Sayeed, M. A., Rouf, H. K., & Hussain, K. M. A. (2020). Effect of thickness on characteristics of ZnSe thin film synthesized by vacuum thermal evaporation. *Journal of Theoretical and Applied Physics*, *14*, 251-259.

[15] Mir, T. A. H., Shaikh, R. A. G., Patil, D. S., & Sonawane, B. K. (2020). Influence of Annealing Temperature Variations on the Properties of Chemically Deposited Nanocrystalline Zinc Selenide Thin Films. *Semiconductors*, *54*(12), 1577-1582.

[16] Hile, D. D., Swart, H. C., Motloung, S. V., Motaung, T. E., Egbo, K. O., & Koao, L. F. (2020). Effect of hydrazine hydrate as complexing agent in the synthesis of zinc selenide thin films by chemical bath deposition. *Thin Solid Films*, *693*, 137707.

[17] Ezenwaka, L. N., Okoli, N. L., Okereke, N. A., Ezenwa, I. A., & Nwori, N. A. (2022). Properties of Electrosynthesized Cobalt Doped Zinc Selenide Thin Films Deposited at Varying Time. *Nanoarchitectonics*, 1-17.

[18] Swathi, S., Rani, B. J., Ravi, G., Yuvakkumar, R., Hong, S. I., Velauthapillai, D., ... & Dang, C. (2020). Designing rational and cheapest SeO2 electrocatalyst for long stable water splitting process. *Journal of Physics and Chemistry of Solids*, *145*, 109544.

[19] Aljeboree, A. M., Abbas, A. S., Abdulrazzak, F. H., Abd Alrazzak, N., & Alkaim, A. F. (2021, September). Role of Selenium dioxide in Spectrophotometric determination of Tetracycline in pure and pharmaceutical formulations. In *Journal of Physics: Conference Series* (Vol. 1999, No. 1, p. 012157). IOP Publishing.

[20] Elshami, W., Tekin, H. O., Al-Buriahi, M. S., Hegazy, H. H., Abuzaid, M. M., Issa, S. A., ... & Zakaly, H. M. (2021). Developed selenium dioxide-based ceramics for advanced shielding applications: Au2O3 impact on nuclear radiation attenuation. *Results in Physics*, *24*, 104099.

[21] Harris, W. I. L. L. I. E. (2008). X-ray Diffraction Techniques. *Methods of Soil Analysis: Mineralogical methods. Part 5*, *9*, 81.

[22] Bunaciu, A. A., UdriŞTioiu, E. G., & Aboul-Enein, H. Y. (2015). X-ray diffraction: instrumentation and applications. *Critical reviews in analytical chemistry*, *45*(4), 289-299.

[23] Waseda, Y., Matsubara, E., & Shinoda, K. (2011). *X-ray diffraction crystallography: introduction, examples and solved problems*. Springer Science & Business Media.

[24] Sands, D. E. (1993). *Introduction to crystallography*. Courier Corporation.

[25] Hammond, C. (2015). *The basics of crystallography and diffraction* (Vol. 21). International Union of Crystal.

[26] Alharbi, S. R., & Qasrawi, A. F. (2018). Gold and ytterbium interfacing effects on the properties of the CdSe/Yb/CdSe nanosandwiched structures. *Current Applied Physics*, *18*(8), 946-951.

[27] Svetikov, V., Ivonin, I., Koshelev, A., Velikov, L., Vorobiev, Y., Goltsov, A., & Yankov, V. (2011, February). Suppression of lateral modes in wide aperture laser diodes by digital planar holograms. In High-Power Diode Laser Technology and Applications IX (Vol. 7918, p. 79180P). International Society for Optics and Photonics.

[28] Qasrawi, A. F., & Aloushi, H. D. (2019). In situ observation of heat-assisted hexagonal-orthorhombic phase transitions in Se/Ag/Se sandwiched structures and their effects on optical properties. Journal of Electronic Materials, 48(12), 7906-7914.

[29] Qasrawi, A. F., & Omareya, O. A. (2019). In situ observations of the permanent structural modifications, phase transformations and band gap narrowing upon heating of Cu2Se/Yb/Cu2Se films. Journal of Alloys and Compounds, 785, 1160-1165.

[30] Fox, M. (2002). Optical properties of solids.

[31] Makuła, P., Pacia, M., & Macyk, W. (2018). How to correctly determine the band gap energy of modified semiconductor photocatalysts based on UV–Vis spectra.

[32] Ghosh A 1990 Physical ReviewB 41 1479[33] Khusayfan, N. M., Qasrawi, A. F., & Khanfar, H. K. (2018). Design and electrical performance of CdS/Sb2Te3 tunneling heterojunction devices. *Materials Research Express*, *5*(2), 026303.

[34] Qasrawi, A. F., & Hamarsheh, A. A. (2021). Design of Au/Cdbr 2/Au as Negative Capacitance Devices and as Band Filters Suitable for 4G Technologies. *Materials Research*, *24*.

[35] Khusayfan, N. M., Qasrawi, A. F., & Khanfar, H. K. (2018). Design and electrical performance of CdS/Sb2Te3 tunneling heterojunction devices. *Materials Research Express*, *5*(2), 026303.

[36] Alharbi, S. R., & Qasrawi, A. F. (2018). Gold and ytterbium interfacing effects on the properties of the CdSe/Yb/CdSe nanosandwiched structures. *Current Applied Physics*, *18*(8), 946-951.

[37] Mickymaray, S. (2019). One-step synthesis of silver nanoparticles using Saudi Arabian desert seasonal plant Sisymbrium irio and antibacterial activity against multidrug-resistant bacterial strains. Biomolecules, 9(11), 662.

[38] Wen, X. J., Niu, C. G., Zhang, L., Liang, C., & Zeng, G. M. (2018). A novel Ag2O/CeO2 heterojunction photocatalysts for photocatalytic degradation of enrofloxacin: possible degradation pathways, mineralization activity and an in depth mechanism insight. Applied Catalysis B: Environmental, 221, 701-714.

[39] Al Garni, S. E., & Qasrawi, A. F. (2017). Effect of Indium nano-sandwiching on the structural and optical performance of ZnSe films. *Results in physics*, *7*, 4168-4173.

[40] Ratsch, C., Seitsonen, A. P., & Scheffler, M. (1997). Strain dependence of surface diffusion: Ag on Ag (111) and Pt (111). *Physical Review B*, *55*(11), 6750.

[41] Caglar, Y., Caglar, M., & Ilican, S. (2018). XRD, SEM, XPS studies of Sb doped ZnO films and electrical properties of its based Schottky diodes. Optik, 164, 424-432.

[42] Yu, Yang, Ruihua Zhao, Juan Chen, and Hong Yao. (2022). "The effect of SO2 on CaO capture selenium in the flue gas: Density functional theory and experimental study." *Chemical Engineering Journal* 431 : 134267.

[43] Naito, Katsuaki, Yasutaka Kuwahara, Hiroko Yamamoto, Yasuhiro Matsuda, Katsushi Okuyama, Takuya Ishimoto, Takayoshi Nakano, Hiromi Yamashita, and Mikako Hayashi. (2022). "Improvement of acid resistance of Zn-doped dentin by newly generated chemical bonds." *Materials & Design* 215 : 110412.

[44] Senocrate, Alessandro, Tolga Acartürk, Gee Yeong Kim, Rotraut Merkle, Ulrich Starke, Michael Grätzel, and Joachim Maier. (2018). "Interaction of oxygen with halide perovskites." *Journal of Materials Chemistry A* 6, no. 23 : 10847-10855.

[45] Zhu, Yu-Ke, Jun Guo, Yi-Xin Zhang, Jian-Feng Cai, Lin Chen, Hao Liang, Shi-Wei Gu, Jing Feng, and Zhen-Hua Ge. "Ultralow lattice thermal conductivity and enhanced power generation efficiency realized in Bi2Te2. 7Se0. 3/Bi2S3 nanocomposites." *Acta Materialia* 218 (2021): 117230.

[46] Schulze, Patricia SC, Karl Wienands, Alexander J. Bett, Saeid Rafizadeh, Laura E. Mundt, Ludmila Cojocaru, Martin Hermle, Stefan W. Glunz, Harald Hillebrecht, and Jan Christoph Goldschmidt. (2020). "Perovskite hybrid evaporation/spin coating method: From band gap tuning to thin film deposition on textures." *Thin Solid Films* 704 : 137970.

[47] Indrakanti, Rajani, V. Brahmaji Rao, and C. Udaya Kiran. (2017). "Studies on conducting nanocomposite with gallium nitride–doped ferrite, part–I." *Proceedings of the Institution of Mechanical Engineers, Part N: Journal of Nanomaterials, Nanoengineering and Nanosystems* 231, no. 1 : 43-52.

[48] Alharbi, Seham R., and Sabah E. Algarni. (2022). "Growth and characterization of (glass, Ag)/SeO2 thin films." *Physica B: Condensed Matter* 633 : 413790.

[49] Alfhaid, L. H. K., & Qasrawi, A. F. (2022). Pt/SeO_2 optical receivers designed for terahertz and 5G/6G technologies. *Physica Scripta*, *97*(5), 055820.

[50] Alharbi, S. R., & Qasrawi, A. F. (2021). Effects of Au nanoslabs on the performance of CdO thin films designed for optoelectronic applications. *Physica E: Low-dimensional Systems and Nanostructures*, *125*, 114386.

[51] Al Garni, S. E., Qasrawi, A. F., & Khusayfan, N. M. (2021). Effects of polycrystalline GeO_2 substrates on the structural, optical and electrical properties of ZnSe thin films. *Physica Scripta*.

[52] Alharbi, S. R., & Algarni, S. E. (2022). Growth and characterization of (glass, Ag)/SeO_2 thin films. *Physica B: Condensed Matter*, *633*, 413790.

[53] Qasrawi, A. F., & Omar, A. (2020). Effects of indium slabs on the structural and electrical properties of stacked layers of Cu2O. *Journal of Ovonic Research Vol*, *16*(2), 83-88.

[54] Alharbi, S. R., & Qasrawi, A. F. (2019). Structural and optoelectronic properties of MoO3/CuSe interfaces. *physica status solidi (a)*, *216*(6), 1800977.

[55] Yin, H., Cao, Y., Fan, T., Qiu, B., Zhang, M., Yao, J., ... & Chen, S. (2020). Construction of carbon bridged TiO2/CdS tandem Z-scheme heterojunctions toward efficient photocatalytic antibiotic degradation and Cr (VI) reduction. *Journal of Alloys and Compounds*, *824*, 153915.

[56] Algarni, S. E., Qasrawi, A. F., & Khusayfan, N. M. (2021). Design and characterization of ZnSe/GeO2 heterojunctions as bandstop filters and negative capacitance devices. *physica status solidi (a)*, *218*(8), 2000830.

تصميم وتوصيف الأجهزة غير المتجانسة $ZnSe / SeO_2$

سوزان خالد سليمان

المشرف أ. عاطف فايز قصراوي

الملخص

في هذه الرسالة قمنا بتصميم وتصنيع فئة جديدة من الأجهزة غير المتجانسة. تستخدم الأغشية الرقيقة n-ZnSe كركائز لتغليف SeO_2- . يتم تحضير الوصلة المشكلة بواسطة تقنية التبخير الحراري تحت ضغط تفريغ 10^{-4} ملي بار. وفقًا لدراسات حيود الأشعة السينية ، تُظهر الأفلام تكدس ZnSe متعدد الكريستالات و SeO_2 غير المتبلور. لإنشاء مخطط نطاق الطاقة لأجهزة $ZnSe / SeO_2$ ، تم تحديد وظيفة عمل SeO_2 بواسطة القياسات الكهربائية. تم أيضًا تحديد فجوات النطاق الخاصة بـــ ZnSe و SeO_2 بشكل تجريبي. وفقًا لمخطط نطاق الطاقة المصمم ، تُظهر الوصلات غير المتجانسة $ZnSe / SeO_2$ إزاحة نطاق التوصيل والتكافؤ 1.91 فولت و 1.61 فولت ، على التوالي. تبلغ إمكانات بناء النطاق المسطح 0.59 فولتًا مما يسمح بتكوين قنوات ترانزستور ذات أغشية رفيعة. عندما يتم طلاء واجهات $ZnSe / SeO_2$ على ركائز معدنية Ag فإنها تظهر خصائص رنانات الميكرو يف. على وجه الخصوص ، أظهر أطياف السعة التي تمت دراستها في مجال التردد 0.1-1.8 جيجاهرتز تأثيرًا سالبًا سالبًا مصحوبًا بظاهرة الرنين والرنين المضاد.

أظهرت نمذجة أطياف السعة باستخدام النماذج الحالية أن طبقة SeO_2 تحسن السعة الهندسية لـــ ZnSe بأكثر من 4 مرات. ؛ لإضافة إلى ذلك ، أظهر التحليل العميق لتوصيل التيار المتردد في مجال تردد الميكروويف أن التيار يهيمن عليه قفز الحاجز المترابط والنفق الميكانيكي الكمومي. تصل كثافة مستويات الفرمي في منطقة الواجهة إلى 10^{18} cm^3 الكترون فولت. علاوة على ذلك ، وجد الجهاز مناسبًا لتصفية إشارة التيار المتردد. تُظهر خصائص مرشح إيقاف النطاق مع قيم خسارة عودة مقبولة ونسب موجة ثابتة للجهد. يمكن أيضًا تصميم أجهزة $Ag / ZnSe / SeO_2$ عن طريق إدخال صفائح نانوية Ag بسماكة 50 نانومتر بين ZnSe و eO_2 . أثر ت هذه الصفائح النانوية سلبًا على الطبيعة متعددة البلورات للأغشية ولكنها تزيل تأثير السعة السلبية للأجهزة. زادت أوراق النانو Ag أيضًا من التوصيل في النطاق الطيفي البالغ

0.5-1.5 جيجا هرتز. تقلل الألواح النانوية Ag من كثافة الحالات بالقرب من مستوى فيرمي بمقد ر أمرين من حيث الحجم. بشكل عام مع هذه الخصائص ، يمكن تسمية واجهات ZnSe / SeO_2 كمرنانات ميكروويف ومصادر سعة سالبة.